NONINVASIVE EVALUATIONS OF SLENDER GRAPHITE RODS AND HUMAN THORACOLUMBAR SPINE

A Dissertation

Presented to the Faculty of the Graduate School

of Cornell University

In Partial Fulfillment of the Requirements for the Degree of

Doctor of Philosophy

by

Ibrahim Erdem

January 2008

NONINVASIVE EVALUATIONS OF SLENDER GRAPHITE RODS AND HUMAN THORACOLUMBAR SPINE

Ibrahim Erdem, Ph.D.

Cornell University 2008

Mechanical properties, internal condition and fracture risk of structural components can be assessed by noninvasive techniques being preferred mainly because of their efficiency and speed. This study presents noninvasive evaluations of slender graphite rods and human thoracolumbar spine. An experimental approach for graphite rods and numerical approaches for both graphite rods and human thoracolumbar spine were developed.

Internal cracks may occur in the graphite rods during the manufacturing process. In an effort to develop a nondestructive testing approach to evaluation of the graphite rods, transient elastic impact was used. Wave theory was used for solid rods. Subsequently, numerical models were developed to determine the response of rods containing cracks. Experiments on graphite rods with and without cracks were conducted and the internal condition was determined from the recorded signals. The rods were then cut lengthwise to reveal the internal condition and verify the predicted results. The knowledge gained from simulations allowed for the presence of cracks to be detected.

For fracture risk assessment of vertebra, finite element (FE) models with simplified geometry, material properties or loading conditions were developed in the past. To investigate the role of these parameters, two FE models were created from CT images:

an isolated L1 vertebra and a T12-L2 spinal segment with ligaments, discs and facets. Each model was examined with both homogeneous and spatially varying bone tissue properties. Stresses and strains were compared for uniform compression and flexion. Inclusion of heterogeneous bone properties and physiological loading in FE models was critical to assess vertebral fracture risk.

The fracture risk of an osteoporotic thoracolumbar junction was assessed using the FE model of L2-T12 spinal segment. Osteoporosis was simulated in four stages, which included disc stiffening and stiffness losses in cancellous core and cortical cortex. Overall stiffness of the segment, and stresses and strains in two sections of L1 were computed for uniform compression and flexion at each stage. This study clearly delineated that osteoporotic bone was at high risk for fracture through not only increased bone stresses and strains with loading, but also changes in the volume and location of bone experiencing these high strains.

BIOGRAPHICAL SKETCH

Ibrahim Erdem was born in Ankara, Turkey, in 1979. He graduated from Middle East Technical University (METU) in June 2001 with a Bachelor of Science in Civil Engineering. He started his graduate studies at METU in September 2001. In August 2003, he was awarded the degree of Master of Science with a major in Structural Engineering. He continued his graduate studies at METU until August 2004 and then he enrolled in Structural Engineering at Cornell University for his Ph.D. degree, with a minor in Mechanical Engineering with an emphasis on Biomechanics. In January 2008, Ibrahim was awarded the degree of Doctor of Philosophy at Cornell University.

ACKNOWLEDGMENTS

I would like to thank Professor Mary Sansalone for her continuous support and invaluable guidance throughout my study. This work could not be completed without her help. I would like to thank Professor Marjolein van der Meulen for her endless support and invaluable guidance on this work. Her enthusiasm for her researches and excellence in her work are very impressive. I also would like to thank Professor Christopher Earls for his guidance, advises and support. I really admire his patience and concern.

I thank Professors Wilkins Aquino and Anthony Ingraffea for their time, concern and comments throughout this study. I also thank Dr. Eeric Truumees for his invaluable comments and input in the clinical aspects of the spine and spinal diseases.

I thank SGL-Carbon for providing the graphite rods, and Tim Bond for maintaining the graphite rods in Winter Lab. I thank Kirk Gunsallus and Jason Long for their time, help and comments during the development of the finite element models. I thank Joseph Lipman for providing CT scan data.

I owe special thanks to my family for their love, support and patience. I also thank my friends with whom I enjoyed memorable time in Ithaca.

TABLE OF CONTENTS

LIST OF FIGURES

LIST OF TABLES

CHAPTER 1

TRANSIENT ELASTIC IMPACT RESPONSE OF SLENDER GRAPHITE RODS[*]

Introduction

Graphite has been used for many applications, including fibers, sheets, plates, structural components, anodes or cathodes. Graphite - with appropriate chemical composition - can also be used as thermal insulator. It is used in nuclear industry to slow down the neutron emitted from the fission or for nuclear transport. Finally, graphite is used in semiconductor and automotive industries. For these different applications, the manufacturing process to produce graphite foils, molded graphite, high purity graphite, and extruded graphite varies. Extruded graphite, which is the focus of this study, is typically circular or rectangular. It is homogenous, having fine grains with low ash content (Table 1.1). To produce extruded graphite calcined petroleum coke is mixed with coal tar pitch. The mixture of green color is then batched into an extrudent to be shaped into rectangular or circular cross sections and with various dimensions. After the extrusion, the graphite specimen is allowed to cool. Subsequently, the graphite rods are baked at about 800°C. Depending on the state of the rod, the baking process may be repeated after adding more pitch. As another alternative, the rod can be treated with an electric current to obtain the desired graphite properties.

During the manufacturing process, three different kinds of internal cracks may occur. In the extrusion phase, cracks with a slightly concaved shape pointing in the direction

[*] Erdem I (2007) Transient elastic impact response of slender graphite rods. Journal of Nondestructive Evaluations. *Under review.*

of the extrusion can occur due to the temperature difference between the mixtures. During the subsequent baking process, flat cracks can occur in a cross-section due to the temperature difference between the interior and exterior part of the graphite rod. The third type of crack being smaller than the other two types is slightly inclined, but flat in shape. This type of crack also occurs during baking process and caused by the contraction of the graphite. It is beneficial to be able to detect the presence of such cracks in the rods prior to their being machined and put into use.

Table 1.1. Properties of graphite

Density	Elasticity Modulus	Poisson Ratio	Compressive Strength	Tensile Strength	Thermal Expansion
1.70 g/cm^3	7-12 GPa	0.2	35-45 MPa	10-13 MPa	2.1-2.6($\times 10^{-6}$) K^{-1}

Impact-echo method and background

The impact-echo method uses transient waves to detect flaws within structures.[1-13] As this method is now well known for its use on other types of geometries, only a very brief explanation is given here and the reader is referred to Sansalone & Streett.[1,2] Short duration, elastic impact is used to generate stress waves in a frequency range appropriate to the dimensions of the structure being tested and the flaws to be detected. A broadband displacement transducer is used to monitor the reflections of these stress waves from the boundaries of the structures and internal cracks. Signals are analyzed in the time and frequency domains (Figure 1.1). The patterns vary with the geometry of the structure and with the presence of discontinuities or flaws within a given geometry.[1-13] In addition, geometrical properties of the member can be obtained such as the dimensions and the locations of the different layers.[1, 3, 4]

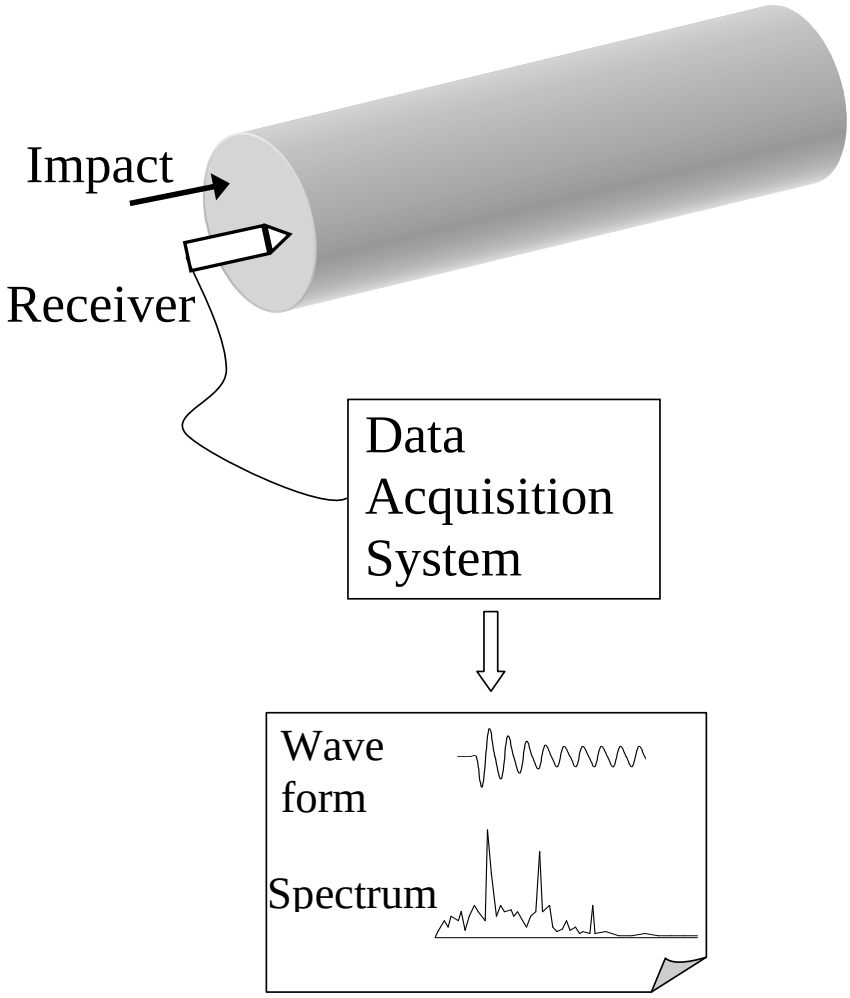

Figure 1.1. Impact-echo testing concept (not scaled)

Using a similar approach (impulse response method) with different sensors (accelerometers) and signal processing techniques, integrity testing of piles has been done for four decades.[14-22] Piles were impacted with a hammer at top and the velocity (or acceleration) was measured to determine the length of the pile and/or approximate location of the flaws. However, because of the length of the piles, duration of the impact, and used sensors, the frequency range obtained and the accuracy of the predictions were low. One dimensional or axisymmetric finite element models were frequently used in those studies.[18-20] However, they did not investigate crack size or

location in detail. Moreover, number of cracks, location of a crack in the transverse section, presence of a longitudinal crack, shape of the crack, the interaction between surface waves and sensing time were not reported. Therefore the results reported in this study would also be helpful for the community interested in non destructive evaluation of piles.

The purpose of this study was three fold: a) to determine the presence of cracks in the graphite rods using numerical and experimental studies since there is no theoretical solution for the rods containing cracks, b) to determine the minimum size of the crack that can be determined, c) to investigate the effects of the shape, number and location of the cracks. To achieve these tasks, wave theory in long bars, eigenvalue and explicit dynamic analyses, and impact-echo testing technique was exploited using the graphite rods with a length to diameter ratio of 13.

Methods

Theory for slender rods

To determine if wave theory for long rods is applicable to the graphite rod case, the frequency content of the solid graphite rods was calculated.[23] For the case of large wave length to bar diameter ratio, the nth frequency can be calculated from

$$f_n = n \cdot c_o / 2L \,, \tag{1}$$

where L is the length of the rod, and c_o is the phase velocity of a bar wave and is calculated from the elasticity modulus (E) and the density (ρ) of the material:

$$c_o = \sqrt{E/\rho} \,. \tag{2}$$

Equation (1) was modified to capture the lateral inertia effect.[23] However, for the slender graphite rod, the change in the frequency due to this correction was small and thus neglected.

Numerical studies

A circular graphite rod with a diameter of 63.5 mm (2.5 inch) and a length of 813 mm (32 inch) was modeled using a commercially-available, finite element (FE) program (ABAQUS, Hibbitt, Karlsson & Sorensen, Inc, RI). The FE model was composed of 12,200 eight-node hexagonal elements (Figure 1.2). Element size (6.6 mm) was selected in such a way that the model could capture the modal frequencies up to 30,000 Hz (15th frequency of the rod).[24] Linearly elastic material properties given in Table 1.1 were used in all analyses since the impact force (1×10^{-6} N) did not cause nonlinear deformation.

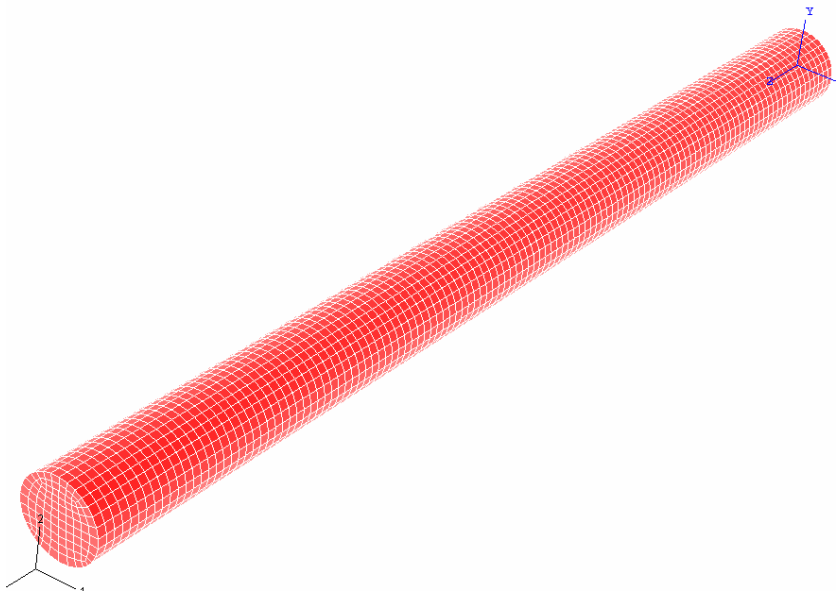

Figure 1.2. Finite element model of the graphite rod

Eigenvalue (modal) analysis was performed using the FE model of the solid rod, without having any restraints, to determine the longitudinal frequencies so that these values could be compared to the theoretical values in Equation (1), and the FE model could be verified. Using the verified FE model, explicit dynamic analysis, which is

suitable for high speed dynamic events such as blast loading and wave propagation, was performed. To do this, an impact force of a half sine curve shaped with contact duration of 30 μs and amplitude of 1×10-6 N was applied at the center of one end (top of the rod). No restraints (free-free) were defined at the ends since all the waves reflect from the ends of the rod. The longitudinal displacement history of a point on the top, which is at 25 mm distance form the impact load, was obtained at every 2 μs for a total analysis time of 4096 μs. Analysis time was set to 4096 μs since a total analysis time of 8192 μs did not change the results significantly (<5%). The data was taken at every 2 μs to capture sufficient longitudinal frequencies. The amplitude spectrum (or longitudinal frequencies) of the rod was obtained by taking Fast Fourier Transformation (FFT) of the displacement data (MATLAB, MathWorks, Inc, MA). Because of the defined boundary condition (free-free) there existed a frequency corresponding to the rigid body motion of the rod, which was discarded from the results.

Explicit dynamic analysis of the rods with cracks was performed in the same way. Both transverse (circular in shape) and longitudinal (rectangular in shape) cracks were investigated. Cracks were created by removing a thin (1 mm) slice within the rod, which would allow the reflections of the bar waves assuming that the cracks completely reflect the bar waves. Cracks with different sizes and shapes, and at different locations were created. Crack size of the transverse cracks was set to either 5,10,14,16,18,20,40,70 and 90% of the cross sectional area of the rod to determine the size effect. These cracks were located at a distance of 80 mm, 340 mm, 406 mm (mid length) or 732 mm from the top of the rod. Transverse cracks were placed either centrally or eccentrically (eccentricity of the crack having an area of 50% of the cross section was 5 mm). Since manufacturing process may cause cracks with different

shapes, flat-, concave- and convex-shaped cracks were investigated (Figure 1.3). Degree of concavity was defined by the ratio of the height (h_c) to depth (d_c) of the crack and was either 0 (flat cracks) or 0.5 or 1.0. Although most of the rod models included just one transverse crack, up to 10 cracks were evenly placed in some models to see the effects of the crack number. A longitudinal crack with different sizes was placed in the center of the rod to determine if impact of the rods at one end could distinguish them. The length of the crack varied from 24.4 mm to 406.5 mm ($0.50\,L$). The width of the crack was between 6.3 mm and 57 mm (90% of the diameter).

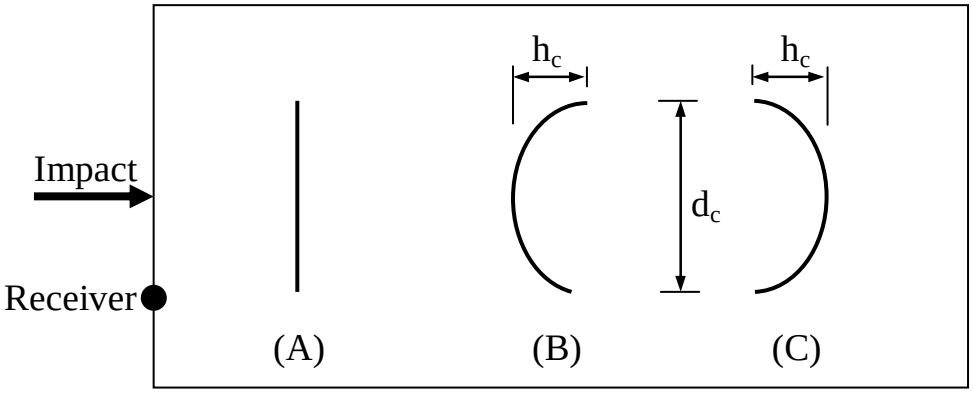

Figure 1.3. Crack shapes analyzed A) flat, B) convex, C) concave

Experimental studies

Eight extruded graphite rods with a length of 852 ± 7 mm and a diameter of 68 ± 1 mm (Table 1.2) was used for the experimental study. One of the rods did not have any cracks in it and was used as reference specimen. Similar to the numerical studies, each specimen was tested in the vertical position by applying a contact force on the top center (Impact-echo technique, Figure 1.1). Data was recorded for 2048 μs, during which normal displacement history of a point on the top surface was monitored using a broadband displacement transducer. The displacement data was then transformed to the frequency domain. Using the frequency content of the rod, the presence and the

location of the crack was predicted. After the tests were completed, the specimens were cut in half lengthwise to observe the internal pattern of the cracks and to check the accuracy of the predictions.

Table 1.2. Tested graphite rods

Specimen	Length / Diameter (mm / mm)	Number of cracks	Maximum crack length (mm)	Depth of the first crack (mm)
ROD 1	849 / 68	9	15	70
ROD 2	850 / 67	6	40	65
ROD 3	847 / 68	10	40	80
ROD 4	851 / 67	8	42	28
ROD 5	851 / 68	12	43	160
ROD 6	845 / 67	4	38	10
ROD 7[a]	859 / 69	-	-	-
ROD 8	849 / 67	9	50	25

[a] Reference specimen

Results and Discussion

Numerical studies

Solid rod

The response of the solid rod in frequency domain obtained from explicit dynamic analysis (Figure 1.4A) and eigenvalue analysis and theory were in good agreement (Table 1.3), implying that the theory for long rods is applicable to the graphite rod problem, and FE model and the numerical and experimental approach for the analysis

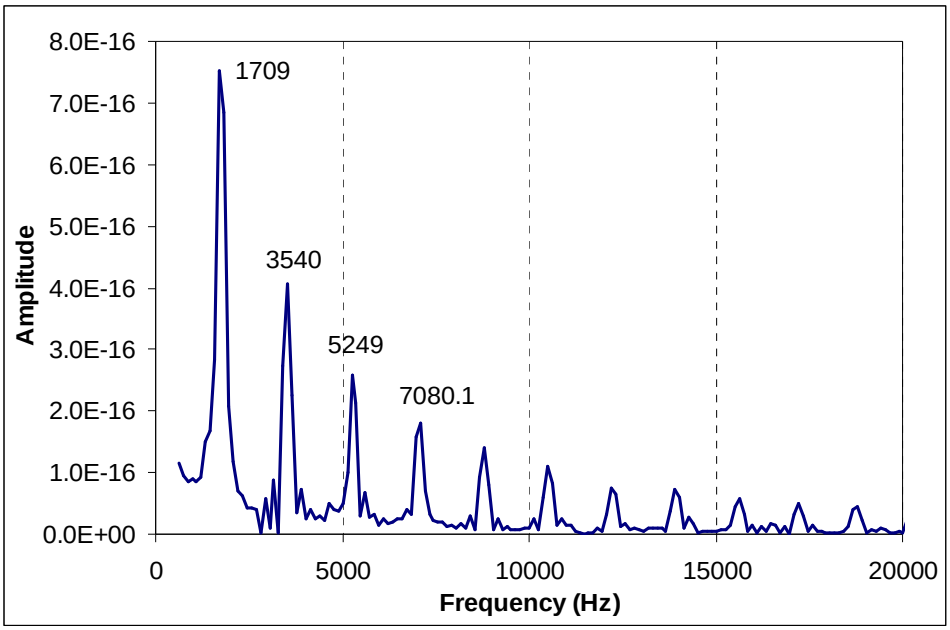

(A)

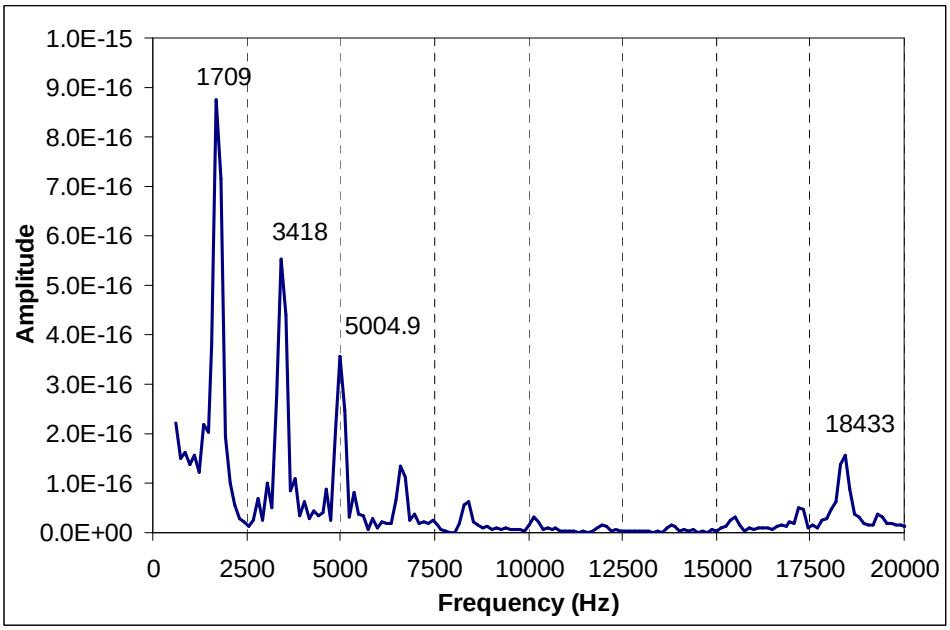

(B)

Figure 1.4. Frequency content (spectrum) of the FE model of the graphite rod, which was obtained by transforming the wave form data in time domain (from explicit dynamic analysis) into frequency domain. Wave form data was calculated at every 2 μs for total 4096 μs. A) solid rod without crack, B) rod with a crack located at a distance of 80 mm from top

of the rods with internal cracks are suitable. The slight deviation of the results from dynamic explicit analysis was due to the accuracy of the amplitude spectrum which is a function of total analysis time. When the total analysis time was increased by 4 folds, the difference between the analytical results and theory became less than 1% (not presented) while the computation time increased by 16 folds. For this reason, the analysis time was set to 4096 μs for other analyses to get accurate results within a reasonable computation time. Finally, the amplitude spectrum of the solid rod (Figure 1.4A) did not change when the impact or measurement locations was changed.

Table 1.3. Longitudinal frequencies of the solid graphite rod

Method	Mode 1 (Hz)	Mode 2 (Hz)	Mode 3 (Hz)	Mode 4 (Hz)
Theory	1765	3530	5296	7061
Eigenvalue	1765	3528	5287	7040
Dynamic Explicit	1709	3540	5249	7080

Crack size

From the crack size analyses it was determined the transverse crack whose size was smaller than 570 mm^2 (18% of the cross section), could not be detected by the stress waves since it did not cause substantial change in the displacement data (wave form) or frequency content of the rod, which is in agreement with previously published studies.[1] As the crack size increases, changes in the wave form and amplitude spectrum becomes more obvious: a) the maximum displacement substantially increased, b) the wave form was more distorted, c) the amplitude of first frequency increased by up to 60%.

Crack location

A crack located at a certain location of the rod caused reflections of the bar waves, causing a resonance frequency, which can be approximately calculated from the following equation:

$$f_{crack} = c_o / 2d \,, \tag{3}$$

where d stands for the depth of the crack. The amplitude of the frequency corresponding to the crack (f_{crack}) had amplitude larger than that of neighboring frequencies (Figure 1.4B), making it possible to determine the presence and location of a crack by looking at the amplitude spectrum of the rod. In addition, the presence of a crack also caused slight shifts in the normal frequencies of the solid rod and the amplitudes of those frequencies, implying that with known response of the solid rod, one can determine the presence of a crack after obtaining the rod's frequency content and the amplitude of the frequencies. Unlike the response of the solid rod, the change in the location of the impact or measurement changed the frequencies and corresponding amplitudes (not shown), meaning that two different analyses or measurements from a rod including an internal crack can reveal the presence of the crack. The change in the frequencies or amplitudes of the modes of solid rod differed depending on the location of the crack (Figure 1.5). For example, the crack located at the mid-length of the rod amplified the even numbered modes of the solid rod without changing the even frequencies since these frequencies are common for the rod length L and $0.5L$. However, the crack located at the mid-length expectedly altered the odd-numbered frequencies of the solid rods. Cracks located other than mid-length caused more changes by affecting almost all frequencies. As obvious from Equation (3), a shallow crack creates a high frequency in the spectrum. Since the element size of the FE model was suitable for frequencies less than 30,000 Hz, a crack located at a depth

of 50 mm or less can not be captured. For this kind of analysis a finer mesh should be used.

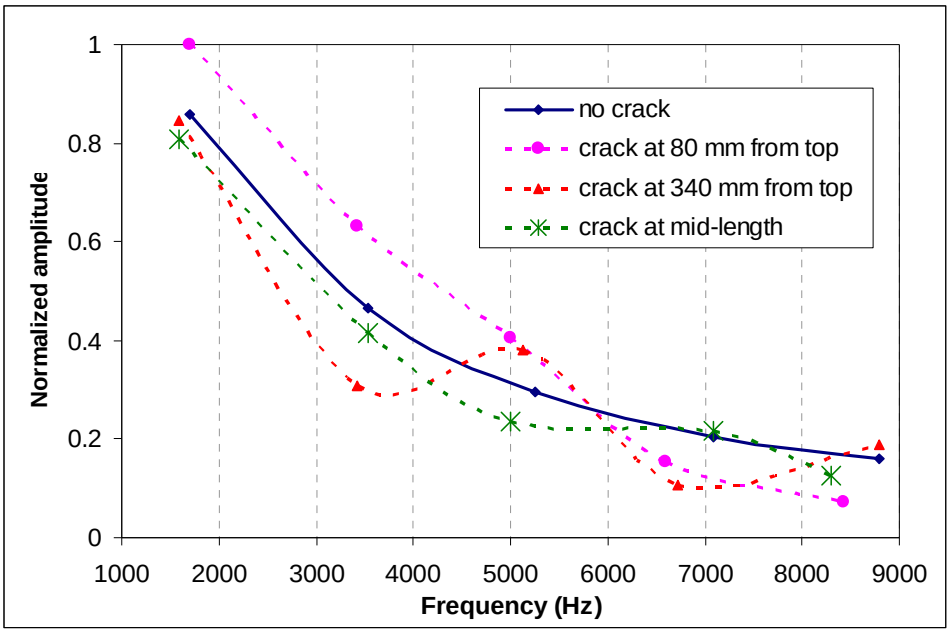

Figure 1.5. Effects of crack location on the frequencies and amplitudes of first five longitudinal modes of the graphite rod. Amplitudes were normalized to the maximum amplitude. Frequencies are marked.

The location of the crack at a certain level also affected the response of the rod. Centered or slightly shifted cracks with the same area produced slightly different spectrums because the shifted crack disturbed the symmetry of the cross section. The difference between the waves forms obtained from centered and shifted cracks were even less, practically none. As the shift of the crack increased, crack got closer to the edge of the rod and caused a flexural mode with low-frequency, high-amplitude (not shown). Because of the high-amplitude flexural frequency, longitudinal frequencies after second mode disappeared (not shown), implying that the invisible cracks extending to the surface of the rods would be easily detected from the frequency content.

Crack number

An increase in the crack number increased the changes in the displacement and frequency patterns of the rod because of the additional wave reflections between the cracks. However, the effects of the crack number were related to the crack size such that when the crack size was much smaller (5% of the cross section) than the minimum detectable size, there was no change in the displacement or frequency pattern, implying that small cracks do not reflect the waves no matter how many of them exist. When the crack size was increased to 16% of the cross section of the rod, the change in the spectrum became obvious with the introduction of three cracks which were evenly spaced along the length of the rod. However, these three cracks only changed the higher (>5th) frequencies. In the case of larger cracks, just one crack was sufficient to easily detect the changes in the response of the rod. Increasing the number of large cracks caused substantial shifts (up to 20%) in the frequencies of the rod. When multiple cracks were present, the crack closest to the impact surface was more readily apparent. Therefore, it may be hard to identify the locations of the cracks below the first crack, unless the first crack is smaller than the second crack. In any case, nicely distributed frequencies of the solid rod are disturbed due to the presence of one or multiple cracks.

Crack shape

It was observed from the amplitude spectrum of the rods that the reflection of the bar waves from a flat crack was more efficient than the reflection from the concave or convex cracks. Therefore as the degree of the concavity increased, the strength of reflections diminished and reduced the effects in the wave form and frequency content. In addition, a concave crack caused slightly more noticeable change than a convex crack with the same size. Therefore, it is more probable to detect a concave

crack than a convex crack and a crack with smaller degree of concavity than a crack with larger degree of concavity.

Longitudinal crack

The longitudinal crack with different sizes did not cause appreciable change in the wave form or spectrum of the solid rod. The maximum change was seen in the amplitude of the first frequency (an increase of 6.7%). Frequency values did not change at all. Therefore, the method involving the impact of the rod at one end can not capture the longitudinal (or split) cracks. Although this type of crack is not observed in extruded graphite rods, it may exist in concrete beams, which should be tested or analyzed under transversely applied impact load.[6,7,11,12]

Wave reflections across the surface

The impact force also produced waves reflected across the surface of the rod. Because the diameter of the rod was small compared to its length, these wave forms were only seen in the initial part of the displacement graphs and the frequency corresponding to these waves was much higher than the longitudinal frequencies. Therefore, for slender rods the waves reflected across the surface is not a problem. However, when the total analysis time was shorter (512 μs), the amplitude of the frequency corresponding to the reflections across the surface becomes apparent as if it corresponded to a crack. For this reason, a sufficient time (>1024 μs) should be allowed for the analysis (or impact-echo test) to eliminate the possible confusion which might be caused by the waves reflected across the surface of the slender rods.

Experimental studies

The spectrum of the graphite rod without any cracks (ROD 7, reference specimen) showed the exact characteristics of a solid rod obtained analytically, that is frequencies were evenly spaced and the amplitudes were inversely proportional to the frequencies. The other rods which had numerous cracks (Table 1.2) gave unevenly spaced frequencies and irregular amplitudes (Figure 1.6), indicating that there were cracks with appreciable sizes in the rods. The wave form of the rods including cracks was also irregular in terms of the occurrence of maximum displacements in time. Investigation of the rods after being cut verified the test results. The depths of the first crack (the one closest to the impacted end) in the rods estimated by using Equation (3) and the frequency emerged was very close to the measured values. Depth of the other cracks was not satisfactorily predicted because of numerous possible reflections between the cracks. Each rod had 4 to 12 cracks in it (Table 1.2) and most of the cracks with lengths ranging from 5 mm to 50 mm were large enough to be detected. ROD 3 and ROD 6 had only flat cracks, and only ROD 8 had one longitudinal crack as a continuation of a transverse crack. All the rods except than the reference rod had different sized and shaped cracks at different locations. Some cracks were located centrally, some eccentrically and some reached to the surface of the rod. Therefore, it was not possible to observe the individual effects of crack size, number and shape. However, ROD 3 and ROD 8 having unfavorable cracks pattern, (many cracks, large cracks and shallow first crack) showed more irregularly distributed frequencies and amplitudes. Thus, impact-echo method can determine the presence of the cracks, the location of the first crack and the severity of the cracks.

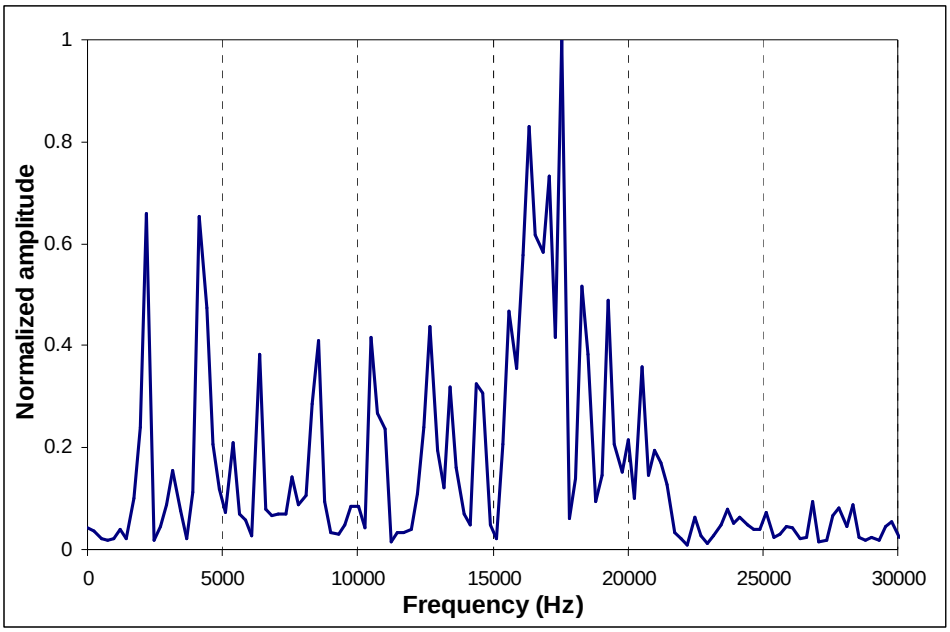

(A)

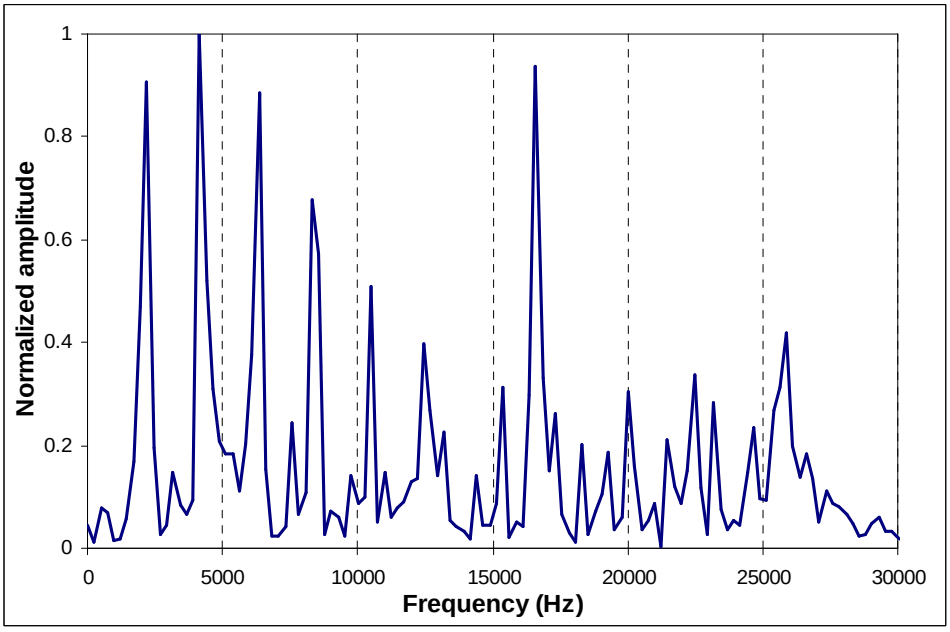

(B)

Figure 1.6. Frequency content (spectrum) of the two test specimens, which was obtained by transforming the wave form data in time domain (from impact-echo test) into frequency domain. Amplitudes were normalized to the maximum amplitude. A) ROD 3, B) ROD 4

Conclusions

This study investigated the effectiveness and capabilities of impact-echo technique on determination of the quality and quantity of internal cracks in slender graphite rods by numerical and experimental studies. Numerical studies provided a complete parametric investigation for crack size, shape, number and location, and the experimental study allowed comparison and verification of the predicted values. As both numerical and experimental studies showed, increasing the number and size of cracks increases the changes in the frequency content of the rod. Crack location determines the frequency content of the rod and the location of the crack closest to the impact can satisfactorily predicted from the amplitude spectrum obtained with impact-echo testing. Although cracks cause changes in the wave forms, the changes in the spectrum (frequency content) are more meaningful and easier to interpret. Longitudinal cracks and cracks whose size is smaller than certain size do not cause remarkable changes on the spectrum. Therefore, transverse impact of the rods for longitudinal rods and other techniques for small cracks can be used. Since all the tested rods, except than the reference specimen, had a large number of internal transverse cracks with remarkable sizes, use of impact-echo technique can achieve nondestructive evaluation of graphite rods and can be a very effective quality control method during the manufacturing process. Although the number of cracks and locations of deeper cracks can not be determined, any specimen that does not show the easily identifiable solid response can be removed from the manufacturing process and use.

REFERENCES

1. Sansalone MJ, Streett WB. Impact-echo. Nondestructive Evaluation of Concrete and Masonry. Bullbrier press, Ithaca, NY; 1997.
2. Sansalone MJ. Impact-echo: The complete story, ACI Structural Journal 1997;94(6):777-86.
3. Sansalone MJ, Lin JM, Streett WB. A new procedure for determining the thickness of concrete highway pavements using surface wave speed measurements and the impact-echo method. Innovations in Nondestructive Testing, Special Publication of ACI; 1996.
4. Sansalone MJ, Carino NJ. Finite element studies of the impact echo response of layered plates containing flaws. International Advances in Nondestructive testing, 15th ed. 313-336. Gordon&Breach Science Publishers, NY; 1990.
5. Sansalone MJ, Carino NJ. Detecting delaminations in reinforced concrete slabs with and without asphalt concrete overlays using the impact-echo method. ACI Materials J 1989;86(2):175-84.
6. Popovics JS, Rose JL. An approach for wave velocity measurement in solid cylindrical rods subjected to elastic impact. Int J Solids Structures 1996;33(26):3925-35.
7. Popovics JS. Effects of Poisson's ratio on impact-echo test analysis. J Eng Mech 1996;123(8):843-51.
8. Sadri A. Application of impact-echo technique in diagnoses and repair of stone masonry structures. NDT & E Int 2003;36(4):195-202.
9. Kesner K, Sansalone MJ, Poston RW. Detection and quantification of distributed damage in concrete using transient stress waves. ACI Materials J 2004;101(4):318-26.
10. Lin Y, Sansalone MJ, Carino NJ. Finite element studies of the transient response of plates containing thin layers and flaws. J Nondestructive Evaluation 1990;9(1):27-47.
11. Lin Y, Sansalone MJ. Transient response of thick rectangular bars subjected to transverse elastic impact. J Acoustical Soc Am 1992;91(5):2674-85.
12. Lin JM, Sansalone MJ. The transient response of hollow cylindrical structures subjected to transverse elastic impact. J Nondestructive Evaluation, 1993;12(2):139-49.
13. Williams TJ, Sansalone MJ, Streett WB, Poston R, Whitlock R. Nondestructive evaluation of masonry structures using the impact-echo method. The Masonry J 1997;15:47-57.

14. Hearne TM, Stokoe KH, Reese LC. Drilled-shaft integrity by wave propagation method, J Geotech Eng ASCE 1981;107(GT10):1327-44.

15. Higgs JS, Robertson SA. Integrity testing of concrete piles by shock method. Concrete. 1979;October:31–33.

16. Davis AG. Nondestructive evaluation of existing deep foundations. J Performance of Constructed Facilities ASCE 1995;9(1):57-74.

17. Finno RJ, Gasman SL. Impulse evaluation of drilled shafts. J Geotech Geoenv Eng ASCE 1998;124(10):965-75.

18. Liao ST, Roesset JM. Dynamic response of intact piles to impulse loads. Int J Numerical and Analytical Methods in Geomechanics 1997;21:255-75.

19. Baxter SC, Islam MO, Gassman SL. Impulse response evaluation of drilled shafts with pile caps: modeling and experiment. Can J Civ Eng 2004;31:169-77.

20. Chow YK, Phoon KK, Chow WF, Wong KY. Low strain integrity testing of piles: three-dimensional effects. J Geotech Geoenv Eng ASCE 2003;129(11):1057–62.

21. Finno RJ, Chao HC. Guided waves in embedded concrete piles. J Geotech Geoenv Eng ASCE 2005;131(1):11-19.

22. Ni SH, Lehmann L, Charng JJ, Lo KF. Low-strain integrity testing of drilled piles with high slenderness ratio. Computers and Geotechnics 2006;33(6-7):283-93.

23. Graff KF. Wave Motion in Elastic Solids. Dover Pub. New York; 1991.

24. ABAQUS 6.5. User's Manual. 1994.

CHAPTER 2

BEHAVIOR OF THE L1 VERTEBRA UNDER DIFFERENT LOADING CONDITIONS[*]

Introduction

Osteoporosis is characterized by low bone mass and altered tissue properties that reduce bone strength and make the skeleton, especially the spine, hip, and wrist, susceptible to fracture under physiological loads. Osteoporosis is responsible for 1.5 million fractures[1] and associated with $18 billion costs annually in the U.S.[1,2] A better understanding of fracture risk is critical to reducing the considerable morbidity and mortality with which osteoporotic fractures are associated. Currently, fracture risk assessment is based on bone mineral density (BMD) measured by dual energy x-ray absorptiometry (DXA).[3] However, substantial overlap exists in the BMD values of individuals who do and do not sustain skeletal fractures[4-9], suggesting a need for alternate approaches of fracture prediction.

Failure of the load-bearing ability of a bone results if the applied load is greater than the strength of the whole bone. In the vertebrae of the spine, for example, loading is applied through the intervertebral disc (IVD), facet joints and ligaments. The structural strength of the vertebrae is determined by the external geometry, cancellous microstructure and tissue material properties. Therefore, the contribution of these factors to loading and bone strength should be taken into account when predicting fracture risk. For engineering structures, finite element (FE) models are routinely used to analyze load-bearing capacity as loading conditions, geometry and material

[*] Erdem I, Truumees E and van der Meulen MCH (2007) Behavior of the L1 vertebra under different loading conditions. Spine. *Under review.*

properties can be incorporated. Thus FE models have the potential to improve clinical predictions of bone fracture by taking the aforementioned factors into account.[6,7,10-31] Moreover, FE models facilitate obtaining the distribution of tissue stresses and strains that cannot be measured experimentally. Hence, FE methods have been used to identify vertebrae at high risk for fracture as well as effects of fracture treatment techniques such as vertebroplasty and kyphoplasty.[28,32-37]

The accuracy and reliability of FE models depend on the specific geometry, material and boundary conditions selected. Simplified geometry, loading or material properties are often implemented to expedite model solution. In many studies cancellous bone is assumed to be a homogenous tissue confined by a stiff cortical shell of constant thickness.[16-20,22-27,33-35,37] Vertebral bodies are often modeled as symmetric around their mid-sagittal section.[18,19,21,26,27,32,34] These simplified models give valuable information on the biomechanics of the spinal motion segments, IVDs and connective tissues, but cannot accurately predict the stress or strain distributions in the vertebral body. FE models that include the heterogeneity of cancellous tissue often simplify the geometry to exclude the posterior processes and IVDs. These simplified loading conditions are appropriate for compressive loading, but limit the ability to simulate flexion-extension, bending and torsional moments.[6,7,10-13,28,32] Since many daily activities impose combined compression and bending on the vertebrae, a single loading condition may not be sufficient for assessing fracture risk.

The objective of this study was to examine the effect of increasing anatomic fidelity in both loading conditions and material properties on FE-based predictions of L1 vertebral stresses and strains under different applied loads. An isolated L1 vertebra loaded through the vertebral body was compared with a motion segment containing

T12-L2 vertebrae with associated IVDs, facet joints and spinal ligaments. To understand the role of material properties on the FE results, each model was examined with homogeneous tissue properties and with spatially varying material properties scaled directly from the bone apparent density. The solutions for the four models were compared under uniform compression and flexion.

Methods

Computed tomography (CT) images from a 55-year-old female cadaver, who had normal bone density and no evident degeneration due to osteoporosis, were used to generate the exact geometry of the T12, L1 and L2 vertebrae. The scans were taken on a clinical scanner (Philips Mx8000 IDT 16) with 1 mm axial slices and 0.453 mm in-plane voxel dimension. The height of all three vertebrae at the center of the body was 26 mm. The height of the IVDs varied through the sagittal section. The cranial IVD (T12-L1) and caudal IVD (L1-L2) had heights of 5.9 mm and 8.5 mm at the center, respectively.

To develop the FE models of the vertebrae, first, the surface geometry of each vertebra was extracted from the CT scan (Mimics, Materialise, Belgium). The resulting geometry consisted of a triangular surface mesh in STL format. Next these surfaces were converted to surface splines in NURBS format (Studio, Raindrop Geomagic, NC). Finally, the surface models were converted to hexagonal FE meshes (Truegrid, XYZ Scientific Applications, CA). A single mesh size was used for all models, based on a mesh refinement analysis. The mesh fineness was determined when the average stresses and strains within the regions of interest differed less than 5% between the coarse mesh and fine mesh. Although the coarse mesh was satisfactory, the fine mesh was used to better capture the geometry of the vertebrae.

Two FE models were created to represent simplified and anatomic boundary conditions (Figure 2.1). The first model, referred to as isolated L1, included only the L1 vertebra with loads applied to the body through polymethylmethacrylate (PMMA) plates on the superior and inferior endplates of L1. The isolated L1 model consisted of 26,452 eight-node hexagonal elements. The second FE model, referred to as T12-L2 spinal motion segment, included three vertebrae (T12, L1 and L2) and two IVDs. The vertebrae and IVDs were modeled with 67,156 eight-noded hexagonal elements. The L1 vertebra was identical to the isolated L1 model. The motion segment included seven structurally relevant ligaments modeled by linear elastic cable elements: anterior longitudinal ligament (ALL), posterior longitudinal ligament (PLL), intertransverse ligament (ITL), supraspinous ligament (SL), interspinous ligament (IL), ligamentum flavum (LF) and capsular ligament (CL) (Table 2.1). The ligament cross-sectional areas and stiffnesses were selected in the range obtained experimentally[38,39] and used previously in the literature.[18,20,25,26] Facet joints between the vertebrae were modeled as frictionless contact surfaces braced with capsular ligaments. In total, 2,752 two-node axial elements were used to model the ligaments and disc fibers in the spinal motion segment.

To model the IVDs, the nucleus pulposus and anulus fibrosis were included. The anulus fibrosis was represented by four layers of stiff fibers embedded in a soft ground material (E=4.2 MPa).[16,18,20,22,24,25] The disc fibers, comprising 19% of the volume of the annulus,[16,22,40] were oriented in a crisscross pattern making an angle, on average, of 30 degrees with the endplates of the vertebrae[16,18,22,24,40] and were also modeled with cable elements. Moving from the inner to the outer anulus layer the spacing between the concentrically placed fibers was reduced by 81% at each layer whereas the cross-sectional area and elastic modulus were increased by 11% to 25%[18,26] to

represent the anisotropy and heterogeneity of the anulus fibrosis (Table 2.1). The nucleus, comprising about 40% of total IVD volume,[20,22,40] was modeled as a nearly incompressible solid with stiffness of 0.2 MPa[25,41] to represent its gelatinous behavior.

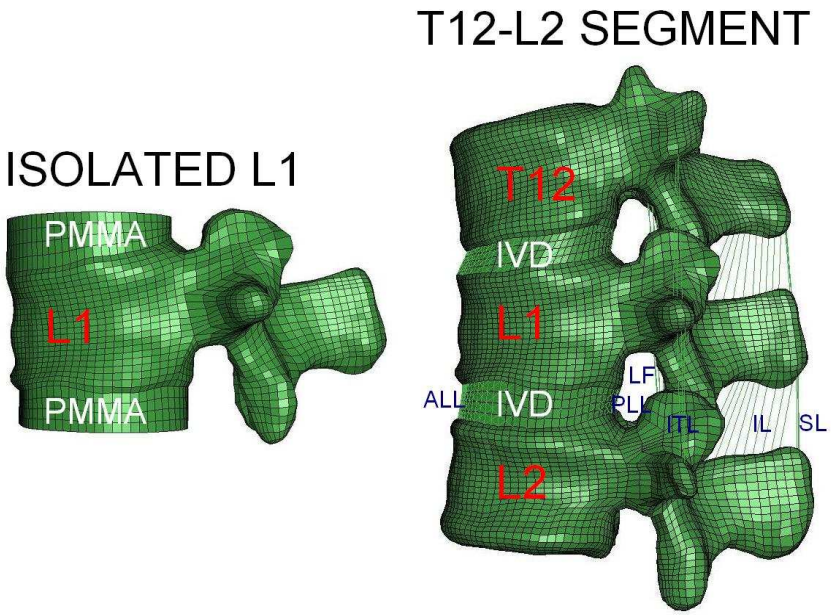

Figure 2.1. Finite element models

For each model two bone material distributions were simulated: an isotropic homogeneous elastic modulus of 1000 MPa, or an isotropic heterogeneous modulus assigned based on an exponential density-elasticity relationship.[42] A linear relationship between the Hounsfield Units (HU), obtained from CT scans, and bone apparent density (ρ, g/cm^3) was utilized:

$$\rho = 0.18 + 0.001244\ (HU-100).$$

The elastic modulus (E, MPa) of the bone tissue was then assigned using the density-elasticity relationship of Morgan et al.:[42]

$$E = 4730\ \rho^{1.56}$$

The moduli ranged from 52 to 7970 MPa and the average elastic modulus in the centrum of the vertebrae varied from 200 to 300 MPa, consistent with the range given for the cancellous bone in the literature (Figure 2.2).[29,30,43-45]

Table 2.1. Ligament and disc fiber properties

	Area (A, mm^2)	**Modulus (E, MPa)**
ALL	64	20
PLL	20	20
ITL	10	50
SL	30	15
IL	40	10
LF	40	20
CL	40	20
Fiber1	0.35	550
Fiber2	0.30	475
Fiber3	0.25	400
Fiber4	0.20	360

ALL: Anterior longitudinal ligament, PLL: Posterior longitudinal ligament, ITL: Inter-transverse ligament, SL: Supraspinous ligament, IL: Interspinous ligament, LF: Ligamentum flavum, CL: Capsular ligament, Fiber1: Outer most anular fiber layer, Fiber4: Innermost anular fiber layer

Two loading cases were investigated for both models: a uniformly distributed compressive force of 400 N or a pure flexion moment with a magnitude of 7.5 Nm applied to the superior endplate. The moment was created by applying concentric forces on the superior end plate of PMMA (isolated L1 model) or T12 (segment

model) while creating zero axial force. Both models were restrained in all directions at the inferior-most endplate. PMMA was modeled as homogenous and isotropic with an elastic modulus of 2,500 MPa and Poisson's ratio of 0.3.

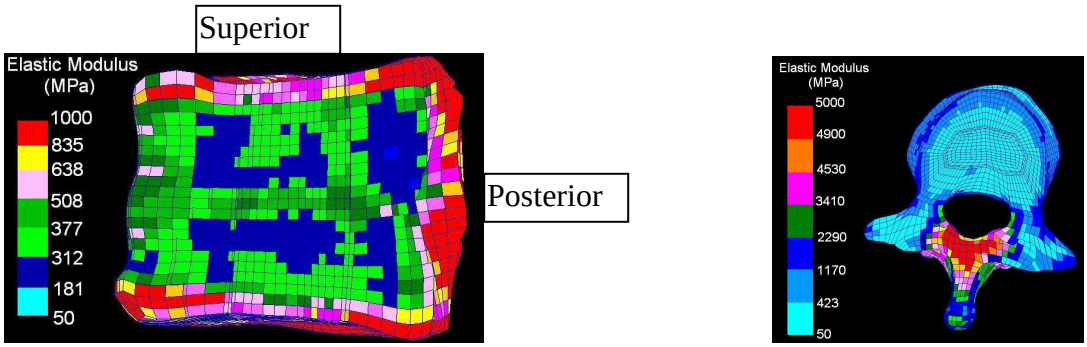

(A) (B)

Figure 2.2. Elastic modulus variation in A) mid-sagittal, B) mid-transverse section of L1

Solutions were obtained using a commercial finite element package (ABAQUS, Hibbitt, Karlsson & Sorensen, Inc, RI). For the isolated vertebra models, we calculated axial and flexion stiffness to characterize the global behavior of the vertebra and to validate our results with previous experimental[31,46,47] and analytical studies.[6,31] For the segment model, we calculated axial displacement in compression, and rotations in flexion and bending to obtain the global behavior and to validate our results with previous experimental[48-53] and analytical[18] studies. The principal stresses and strains, and von Mises stresses in the mid-transverse and mid-sagittal sections of the L1 vertebra were compared across boundary conditions and material properties.

Results

To validate the isolated L1 model with heterogeneous bone properties, we calculated an axial stiffness of 14 kN/mm, similar to several previous studies[6,46] but larger than

other studies (2 to 9.7 KN/mm).[31,47] The measured variation in the axial stiffness of the isolated vertebra may result from differences in test protocols, the presence or absence of posterior elements, and the specimen age, condition and vertebra level.

For validation of the segment model, an axial displacement of 0.52 mm was calculated in compression, comparable with the values in the literature.[48] The average bulging was 0.21 mm and 0.31 mm for the cranial and caudal IVDs, respectively, in the range reported previously.[53] In flexion and bending, 3.2 and 4.3 degree rotation was obtained, respectively, in the range obtained from previous studies.[18,48,50-52]

When the heterogeneity of the bone tissue was not included, the distributions of the stresses and strains of the isolated vertebra were affected only by the loading and external geometry. The asymmetric shape of the vertebral body and the irregular curvature of the superior and inferior endplates contributed to variations in the stress and strain distributions in the cross sections under applied compression (Figures 2.3 and 2.4). Although the compressive load was uniformly distributed, the anterior side of L1 was subjected to higher stresses and strains than the posterior aspect. The largest minimum principal strain and the maximum von Mises stress in the mid-transverse section occurred at the left lateral cortex of the vertebral body (Table 2.2). When the isolated homogeneous vertebra was loaded in flexion, stress and strain distributions were similar to those of a homogenous beam under flexure (Figure 2.5), i.e., the stresses and strains were highest at the anterior and posterior sides of the vertebral body and lowest at the center (Table 2.3).

Accounting for material heterogeneity changed the mechanical behavior of the L1 vertebra. The axial and flexion stiffness of the L1 vertebra were reduced by 55% and

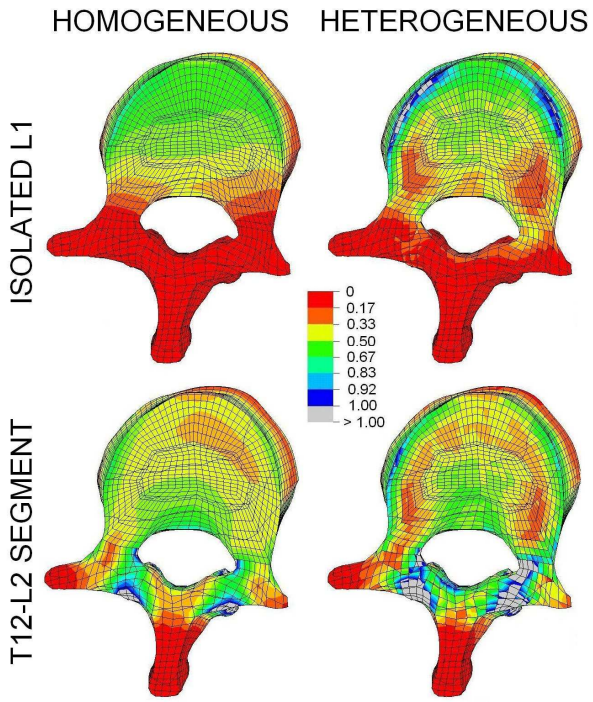

Figure 2.3. von Mises stresses (in MPa) in the mid-transverse section due to compression

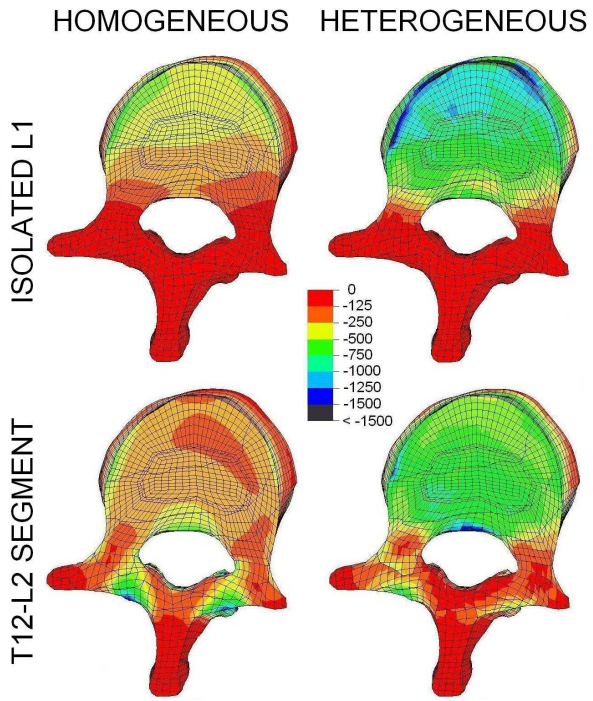

Figure 2.4. Minimum principal strains (in microstrains) in the mid-transverse section due to compression

Table 2.2. von Mises stresses and minimum principal strains at the center, posterior, anterior, left and right cortex of the mid-transverse section of L1 under compression. L1 = isolated vertebral body model; T12-L2 = motion segment model; homo = homogeneous bone properties; hetero = heterogeneous bone properties.

	L1 homo	L1 hetero	T12-L2 homo	T12-L2 hetero	% difference between L1 homo and T12-L2 hetero
Von Mises stresses (MPa)					
center	0.385	0.330	0.307	0.335	-13
posterior	0.263	0.189	0.612	0.383	46
anterior	0.423	0.477	0.236	0.258	-39
left	0.555	0.805	0.492	0.665	20
right	0.407	0.538	0.347	0.467	15
Minimum principal strains (microstrain)					
center	-390	-837	-288	-767	97
posterior	-266	-634	-585	-1187	346
anterior	-421	-1002	-237	-518	23
left	-577	-1296	-513	-1021	77
right	-392	-906	-358	-743	90

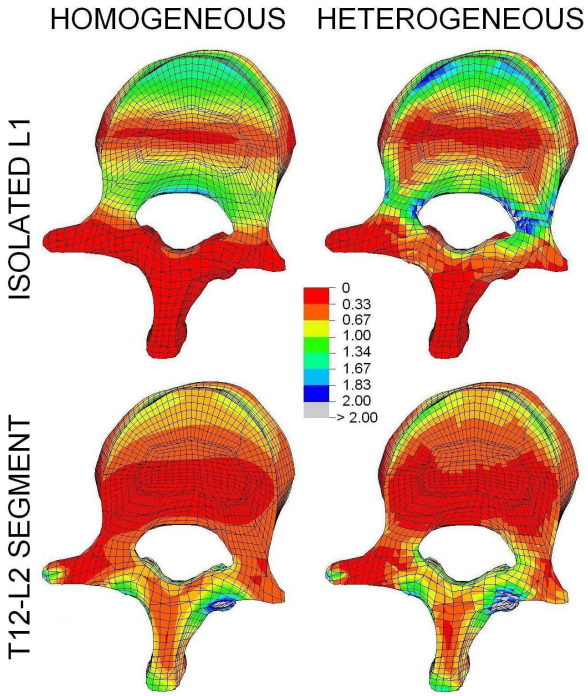

Figure 2.5. von Mises stresses (in MPa) in the mid-transverse section due to flexion

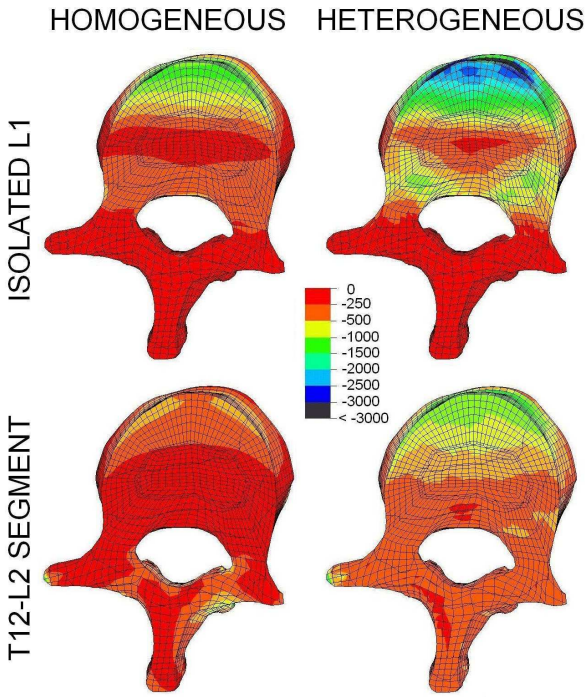

Figure 2.6. Minimum principal strains (in microstrains) in the mid-transverse section due to flexion

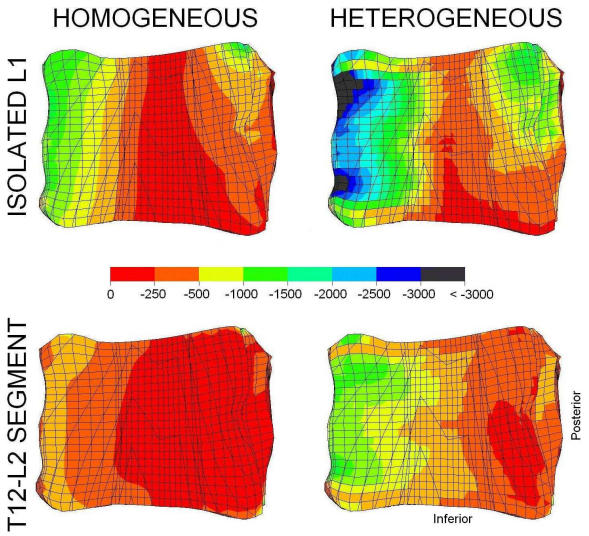

Figure 2.7. Minimum principal strains (in microstrains) in the mid-sagittal section due to flexion

Table 2.3. von Mises stresses and minimum principal strains at the center, posterior, anterior, left and right cortex of the mid-transverse section of L1 in flexion. L1 = isolated vertebral body model; T12-L2 = motion segment model; homo = homogeneous bone properties; hetero = heterogeneous bone properties.

	L1 homo	L1 hetero	T12-L2 homo	T12-L2 hetero	% difference between L1 homo and T12-L2 hetero
Von Mises stresses (MPa)					
center	0.124	0.100	0.174	0.181	46
posterior	1.43	0.758	0.250	0.092	-94
anterior	1.24	1.18	0.484	0.472	-62
left	0.203	0.316	0.309	0.338	67
right	0.284	0.358	0.213	0.178	-37
Minimum principal strains (microstrain)					
center	-115	-269	-166	-429	273
posterior	-446	-623	-78	-58	-87
anterior	-1227	-2428	-479	-953	-22
left	-202	-503	-327	-566	180
right	-273	-597	-214	-313	15

39%, respectively. Heterogeneity of the bone tissue also altered the distributions of stresses and strains in the mid-transverse and mid-sagittal sections of L1 for compression. The minimum principal strain in the mid-transverse section exceeded the homogeneous maximum value at the left and right lateral and anterior cortex by at least 125%. Moreover, the largest von Mises stress in the mid-transverse section increased by 45% at the left cortex (Table 2.2). Although the heterogeneous and homogeneous L1 models had similar stress profiles on the superior endplates, the regions of high stresses and strains were altered. Heterogeneity of the bone tissue caused both stress relief and increased stresses and resulted in a slight shift of the stresses towards the pedicles (Figure 2.3). The inclusion of heterogeneity caused relatively more dramatic changes in the distributions of the stresses and strains for flexion (Figures 2.5-2.7). Although the highest stresses and strains occurred at the anterior and posterior sides of the vertebral body, the change in the minimum principal strain was greatest at the center of the vertebral body (134%) (Table 2.3). The changes in the minimum principal strains were almost always higher than the changes in the von Mises stresses (Table 2.3). In the mid-sagittal section, the highest minimum principal strains shifted from the anterior superior endplate to just above and below the mid-anterior cortex of the vertebra (Figure 2.7).

The stress and strain distributions changed further when physiological loading was applied to L1 through T12 and L2, the intervertebral discs, ligaments and facets. In compression, although the facets and capsular ligaments contributed to the load transfer, the disc mainly transferred the load to the neighboring vertebra. Including the capsular ligaments and facet joints shifted the stresses towards the posterior side of the vertebra (Figure 2.3). The minimum principal strain at the anterior lamina at the mid-transverse section of the homogenous model increased 11.8–fold with the more

physiological loading (Figure 2.4). The maximum change in both von Mises stresses and minimum principal strains occurred in the posterior cortex of the mid-transverse section with more severe changes in the strains (Table 2.2). The stresses and strains at the left cortex in the mid-transverse section were at least 29% larger than those at the right cortex (Table 2.2). Although the inclusion of heterogeneous bone properties did not change the overall displacements or rotations of the vertebrae (less than 5%), the strains were affected more than the stresses (Figures 2.3 and 2.4). The von Mises stresses at the center and anterior of the mid-transverse section increased by only 9% (Table 2.2). However, the minimum principal strains increased by 99% to 166% in all five regions with heterogeneous bone properties (Table 2.2).

The physiological loading had remarkable effects on the response of L1 when the segment was loaded in flexion. Facets and all ligaments, except the anterior longitudinal ligament, played a significant role in the load transfer mechanism. In the mid-transverse section, stresses and strains shifted from the posterior vertebra towards the laminas (Figures 2.5 and 2.6). Both von Mises stress and minimum principal strain in the anterior cortex in the mid-transverse section reduced by 61% (Table 2.3). In the mid-sagittal section of the segment, the high stresses and strains observed in the anterior cortex of the isolated vertebra body reduced and the minimum principal strains at the superior posterior wedge diminished (Figure 2.7). Unlike the isolated vertebra in flexion, the stresses and strains in the mid-transverse section were at least 31% higher in the left cortex than right cortex (Table 2.3). As in compression, the heterogeneity of the bone tissue did not significantly change the overall displacements or rotations of the vertebra (less than 5%) but did change the stresses and strains. The change in the minimum principal strains was more severe than that of the von Mises stresses in the mid-transverse section (Table 2.3). In the segment models, including

heterogeneous bone properties increased the minimum principal strain by 61% and 50% in at the center and anterior of mid-transverse section compared to the homogenous case (Table 2.3, Figure 2.6). In addition, the inclusion of heterogeneity in the segment model increased the minimum principal strains in the inferior endplate in the mid-sagittal section under flexion (Figure 2.7).

Discussion

In this study, we investigated the effects of heterogeneity of bone tissue and physiological loading on stress and strain predictions in the L1 vertebra using FE models. Not surprisingly, different material properties and loading conditions resulted in changes in the stresses and strains up to 346% in the transverse and sagittal sections examined. In compression, the changes in both stresses and strains were most pronounced in the posterior of the vertebral body, whereas in flexion the most-affected-region varied depending on the outcome parameter, and material or loading conditions. In general stresses were affected more by the loading conditions, whereas changing the material properties substantially altered the strains. The overall changes across the models were most pronounced in flexion. In the laboratory, bone tissue failure is dependent on the applied strain levels,[12,13,46] underscoring the need for accurate local strains to predict failure.

For our investigation, we chose the thoracolumbar junction (T12 to L2) as osteoporotic fractures occur most frequently here and in the mid-thoracic spine.[4,54,55] To the best of our knowledge, no detailed model of the thoracolumbar motion segment has been developed. The model developed by Villarraga et al. included the T12-L2 segment but did not include posterior elements or ligaments, affecting the accuracy under flexural loading.[34] Qiu et al. modeled T12-L1 with posterior elements while

fixing the L1 vertebra at its inferior endplate, which resulted in the loss of the physiological boundary condition (IVD) at the bottom of L1.[24] Many studies have analyzed isolated vertebral bodies in the thoracolumbar junction without simulating physiological loading.[6,7,10-13,28] Our results show that both the values and distribution of stresses and strains are very different when physiological loading is applied, affecting both failure location and timing. Therefore, we expect our heterogeneous segmental model to better predict the apparent stresses and strains produced in the vertebra with compressive and flexural loading.

Previous models of spinal segments[16-27,33-35,37] focused mainly on the behavior of the IVD, ligaments and facets, and model these structures in detail, or the overall mechanics of the motion segment. As our results show, overall behavior of the spinal segment with and without heterogeneous bone properties did not change. Among the spinal segment models, stress or strain values in the vertebrae, can be directly compared to our results.[17,18,22,24,25,33,34] These models were created using different levels in the lumbar spine and reported stresses or strains under different load magnitudes. When scaled appropriately, our results are in agreement with several models[17,18,34] but our values are substantially lower than others.[22,25,33] We attribute the differences across models to different material models for the cortical shell, homogeneous cancellous bone properties, and differences in the geometry and level of the vertebra.

In light of the above discussion the most significant strengths of our study are the incorporation of heterogeneous bone properties and physical boundary conditions for the stress analysis of the L1 vertebra. While homogeneous bone properties isolate the effects of geometry, loading and boundary conditions on vertebral stresses and strains,

the material properties determine the load sharing (or stress distribution) within the vertebral tissue. Our strain distributions changed substantially due to the spatial variation of the elastic modulus of the bone which will affect fracture risk prediction. The stress distribution in L1 when loaded through a PMMA plate was remarkably different than loaded through IVDs, ligaments and facets due to several factors. In the segment model the vertebra was constrained by flexible IVDs, unlike the loading through less flexible plates in the isolated vertebra model. The material property differences between the homogeneous, isotropic PMMA and the heterogeneous, anisotropic IVD also contribute to the differences we observed. Finally, the posterior processes play an important role in load sharing during flexion of the segment.

The incorporation of patient specific, vertebral geometry and material properties is another strength of our approach. Modeling the vertebra with symmetry, average geometry or flat endplates will underestimate stresses and strains and change the load paths. Therefore, for better fracture risk assessment, true geometry of the vertebra should be used. In addition, our model better captures the true geometry than isolated vertebral models developed from CT scans[6,7,10] that use voxel-based elements causing a loss in the accuracy of the true geometry and the cortical shell. However, our model development is not as automated as in the voxel-based approach.

Our models have some limitations. We did not include viscosity, porosity and nonlinearity of the materials. Therefore, impact or time dependent loading can not be simulated. Due to these simplifications, we also can not capture the full mechanical behavior of the motion segment. Bone tissue is not isotropic[56-59] and we excluded the orthotropic (or transversely isotropic) behavior of the bone tissue in our model, which

may underestimate the transverse stresses and strains. Finally, our conclusions are based on a data from a single individual.

A more detailed understanding of areas of vulnerability under loading will provide insights into failure locations and improve efforts towards reconstruction after fracture and fixation of osteoporotic vertebral bodies. Since current clinical methods cannot predict individuals who will fracture or respond to treatment, patient specific FE models provide an opportunity to mechanistically understand and predict vertebral failure. As our results show, including heterogeneity of the vertebra, and physiological boundary conditions and loading are critical to determining the locations and distribution of highly loaded tissue that is at risk for failure. We have demonstrated these effects in a normal spine; the distributions and magnitudes of the stresses and strains will change further when material changes are present because of osteoporosis. In addition, treatments such as vertebroplasty, kyphoplasty, spinal fusion and disc replacement will change vertebral load transfer and therefore fracture risk. To truly understand the effects such treatments have on the vertebra and select appropriate treatments, FE models need to incorporate patient specific material properties in conjunction with realistic loading conditions.

REFERENCES

1. U.S. Department of Health and Human Services. Health and Osteoporosis: A Report of the Surgeon General. Rockville, MD: Department of Health and Human Services, Office of the Surgeon General; 2004
2. Tosteson AN, Hammond CS. Quality-of-life assessment in osteoporosis: health-status and preference-based measures. Pharmacoeconomics 2002;20:289-303.
3. Gustafsson L, Jacobson B, Kusoffsky L. X ray spectrophotometry for bone-mineral determinations. Med Biol Eng 1974;12:113-9.
4. Melton LJ, 3rd, Kan SH, Frye MA, et al. Epidemiology of vertebral fractures in women. Am J Epidemiol 1989;129:1000-11.
5. Cauley JA, Zmuda JM, Wisniewski SR, et al. Bone mineral density and prevalent vertebral fractures in men and women. Osteoporos Int 2004;15:32-7.
6. Crawford RP, Cann CE, Keaveny TM. Finite element models predict in vitro vertebral body compressive strength better than quantitative computed tomography. Bone 2003;33:744-50.
7. Faulkner KG, Cann CE, Hasegawa BH. Effect of bone distribution on vertebral strength: assessment with patient-specific nonlinear finite element analysis. Radiology 1991;179:669-74.
8. Kanis JA, Borgstrom F, De Laet C, et al. Assessment of fracture risk. Osteoporos Int 2005;16:581-9.
9. Schuit SC, van der Klift M, Weel AE, et al. Fracture incidence and association with bone mineral density in elderly men and women: the Rotterdam Study. Bone 2004;34:195-202.
10. Crawford RP, Keaveny TM. Relationship between axial and bending behaviors of the human thoracolumbar vertebra. Spine 2004;29:2248-55.
11. Liebschner MA, Kopperdahl DL, Rosenberg WS, et al. Finite element modeling of the human thoracolumbar spine. Spine 2003;28:559-65.
12. Silva MJ, Keaveny TM, Hayes WC. Computed tomography-based finite element analysis predicts failure loads and fracture patterns for vertebral sections. J Orthop Res 1998;16:300-8.
13. Kopperdahl DL, Roberts AD, Keaveny TM. Localized damage in vertebral bone is most detrimental in regions of high strain energy density. J Biomech Eng 1999;121:622-8.
14. van der Linden JC, Birkenhager-Frenkel DH, Verhaar JA, et al. Trabecular bone's mechanical properties are affected by its non-uniform mineral distribution. J Biomech 2001;34:1573-80.

15. Kosmopoulos V, Keller TS. Finite element modeling of trabecular bone damage. Comput Methods Biomech Biomed Engin 2003;6:209-16.

16. Natarajan RN, Andersson GB. The influence of lumbar disc height and cross-sectional area on the mechanical response of the disc to physiologic loading. Spine 1999;24:1873-81.

17. Noailly J, Lacroix D, Planell JA. Finite element study of a novel intervertebral disc substitute. Spine 2005;30:2257-64.

18. Shirazi-Adl A, Ahmed AM, Shrivastava SC. A finite element study of a lumbar motion segment subjected to pure sagittal plane moments. J Biomech 1986;19:331-50.

19. Ueno K, Liu YK. A three-dimensional nonlinear finite element model of lumbar intervertebral joint in torsion. J Biomech Eng 1987;109:200-9.

20. Chen CS, Cheng CK, Liu CL, et al. Stress analysis of the disc adjacent to interbody fusion in lumbar spine. Med Eng Phys 2001;23:483-91.

21. Goel VK, Clausen JD. Prediction of load sharing among spinal components of a C5-C6 motion segment using the finite element approach. Spine 1998;23:684-91.

22. Guo LX, Teo EC, Lee KK, et al. Vibration characteristics of the human spine under axial cyclic loads: effect of frequency and damping. Spine 2005;30:631-7.

23. Wang JL, Parnianpour M, Shirazi-Adl A, et al. Viscoelastic finite-element analysis of a lumbar motion segment in combined compression and sagittal flexion. Effect of loading rate. Spine 2000;25:310-8.

24. Qiu TX, Tan KW, Lee VS, et al. Investigation of thoracolumbar T12-L1 burst fracture mechanism using finite element method. Med Eng Phys 2006;28:656-64.

25. Polikeit A, Nolte LP, Ferguson SJ. The effect of cement augmentation on the load transfer in an osteoporotic functional spinal unit: finite-element analysis. Spine 2003;28:991-6.

26. Maurel N, Lavaste F, Skalli W. A three-dimensional parameterized finite element model of the lower cervical spine. Study of the influence of the posterior articular facets. J Biomech 1997;30:921-31.

27. Goel VK, Park H, Kong W. Investigation of vibration characteristics of the ligamentous lumbar spine using the finite element approach. J Biomech Eng 1994;116:377-83.

28. Liebschner MA, Rosenberg WS, Keaveny TM. Effects of bone cement volume and distribution on vertebral stiffness after vertebroplasty. Spine 2001;26:1547-54.

29. van Lenthe GH, Stauber M, Muller R. Specimen-specific beam models for fast and accurate prediction of human trabecular bone mechanical properties. Bone 2006;39:1182-9.

30. Kopperdahl DL, Keaveny TM. Yield strain behavior of trabecular bone. J Biomech 1998;31:601-8.

31. Buckley JM, Loo K, Motherway J. Comparison of quantitative computed tomography-based measures in predicting vertebral compressive strength. Bone 2007;40:767-74.

32. Tschirhart CE, Roth SE, Whyne CM. Biomechanical assessment of stability in the metastatic spine following percutaneous vertebroplasty: effects of cement distribution patterns and volume. J Biomech 2005;38:1582-90.

33. Zander T, Rohlmann A, Klockner C, et al. Effect of bone graft characteristics on the mechanical behavior of the lumbar spine. J Biomech 2002;35:491-7.

34. Villarraga ML, Bellezza AJ, Harrigan TP, et al. The biomechanical effects of kyphoplasty on treated and adjacent nontreated vertebral bodies. J Spinal Disord Tech 2005;18:84-91.

35. Baroud G, Nemes J, Heini P, et al. Load shift of the intervertebral disc after a vertebroplasty: a finite-element study. Eur Spine J 2003;12:421-6.

36. Keller TS, Kosmopoulos V, Lieberman IH. Vertebroplasty and kyphoplasty affect vertebral motion segment stiffness and stress distributions: a microstructural finite-element study. Spine 2005;30:1258-65.

37. Rohlmann A, Zander T, Bergmann G. Spinal loads after osteoporotic vertebral fractures treated by vertebroplasty or kyphoplasty. Eur Spine J 2006;15:1255-64.

38. Pintar FA, Yoganandan N, Myers T, et al. Biomechanical properties of human lumbar spine ligaments. J Biomech 1992;25:1351-6.

39. Chazal J, Tanguy A, Bourges M, et al. Biomechanical properties of spinal ligaments and a histological study of the supraspinal ligament in traction. J Biomech 1985;18:167-76.

40. White A, Panjabi M. Biomechanics of the Spine. Philadelphia: JB Lippincott; 1990.

41. Sharma M, Langrana NA, Rodriguez J. Role of ligaments and facets in lumbar spinal stability. Spine 1995;20:887-900.

42. Morgan EF, Bayraktar HH, Keaveny TM. Trabecular bone modulus-density relationships depend on anatomic site. J Biomech 2003;36:897-904.

43. Morgan EF, Keaveny TM. Dependence of yield strain of human trabecular bone on anatomic site. J Biomech 2001;34:569-77.

44. Uchiyama T, Tanizawa T, Muramatsu H, et al. Three-dimensional microstructural analysis of human trabecular bone in relation to its mechanical properties. Bone 1999;25:487-91.

45. Cendre E, Mitton D, Roux JP, et al. High-resolution computed tomography for architectural characterization of human lumbar cancellous bone: relationships with histomorphometry and biomechanics. Osteoporos Int 1999;10:353-60.

46. Kopperdahl DL, Pearlman JL, Keaveny TM. Biomechanical consequences of an isolated overload on the human vertebral body. J Orthop Res 2000;18:685-90.

47. Heini PF, Berlemann U, Kaufmann M, et al. Augmentation of mechanical properties in osteoporotic vertebral bones--a biomechanical investigation of vertebroplasty efficacy with different bone cements. Eur Spine J 2001;10:164-71.

48. Schultz A, Warwick W, Berkson M, et al. Mechanical properties of human lumbar spine motion segments. Part I: Responses in flexion, extension, lateral bending, and torsion. J Biomech Eng 1979;101:46-52.

49. Berkson M, Nachemson A, Schultz A. Mechanical properties of human lumbar spine motion segments. Part II: Responses in compression and shear; influence of gross morphology. J Biomech Eng 1979;101:53-57.

50. Goel VK, Goyal S, Clark C, et al. Kinematics of the whole lumbar spine. Effect of discectomy. Spine 1985;10:543-54.

51. Panjabi MM, Oxland TR, Yamamoto I, et al. Mechanical behavior of the human lumbar and lumbosacral spine as shown by three-dimensional load-displacement curves. J Bone Joint Surg Am 1994;76:413-24.

52. Panjabi MM, Krag MH, Chung TQ. Effects of disc injury on mechanical behavior of the human spine. Spine 1984;9:707-13.

53. Frei H, Oxland TR, Rathonyi GC, et al. The effect of nucleotomy on lumbar spine mechanics in compression and shear loading. Spine 2001;26:2080-9.

54. Melton LJ, 3rd, Wahner HW. Defining osteoporosis. Calcif Tissue Int 1989;45:263-4.

55. Cooper C, Atkinson EJ, O'Fallon WM, et al. Incidence of clinically diagnosed vertebral fractures: a population-based study in Rochester, Minnesota, 1985-1989. J Bone Miner Res 1992;7:221-7.

56. Mosekilde L, Danielsen CC. Biomechanical competence of vertebral trabecular bone in relation to ash density and age in normal individuals. Bone 1987;8:79-85.

57. Ulrich D, van Rietbergen B, Laib A, et al. The ability of three-dimensional structural indices to reflect mechanical aspects of trabecular bone. Bone 1999;25:55-60.

58. Galante J, Rostoker W, Ray RD. Physical properties of trabecular bone. Calcif Tissue Res 1970;5:236-46.

59. Burstein AH, Reilly DT, Martens M. Aging of bone tissue: mechanical properties. J Bone Joint Surg Am 1976;58:82-6.

CHAPTER 3

FRACTURE RISK OF THE OSTEOPOROTIC THORACOLUMBAR SPINE*

Introduction

Spinal and other fractures and their attendant morbidity and mortality occur frequently in elderly population. Although a sharp increase in load may cause traumatic fracture, spinal fractures generally occur during activities of daily living such as lifting and bending,[1,2] implying that the main cause of the fracture is reduction of the vertebral strength. The strength reduction is caused by altered bone mass and geometry which can be associated with osteoporosis.[3-6] Among these changes, the thinning and disintegration of trabeculae, reduced cortical thickness and increased porosity caused by the reduced mineral content and altered collagen quantity and quality are frequently mentioned. Hence, stiffness and strength loss of both cancellous bone[7-17] and the cortical shell[18,19] have been investigated. Patients with osteoporosis also have disc degeneration,[20] characterized by loss of fluidity and incompressibility of nucleus pulposus, stiffening of anulus fibrosis and loss of clear boundary between nucleus and anulus.[12,21-30] Degenerated and stiffened intervertebral disc (IVD) will cause a change in physical loading of vertebra by altering the stress distribution at the vertebral endplates.

Osteoporotic fractures, which reduce the overall quality of life,[31-33] are responsible for $18 billion annual costs in the U.S.[33,34] Therefore diagnosis of osteoporosis and prediction of fracture risk are essential to allow preventive measures to be taken or to decide if the patient needs surgery. Clinically, bone mineral density (BMD) measured

* Erdem I, Truumees E and van der Meulen MCH (2007) Fracture risk of the osteoporotic thoracolumbar spine. *In preparation.*

by dual energy x-ray absorptiometry (DXA) is used to diagnose osteoporosis and related fracture risk.[35] However, BMD by itself does not satisfactorily predict fracture,[10,36-42] suggesting a need for alternate approaches for fracture risk assessment. Since finite element (FE) modeling can incorporate physical loading conditions and geometry beyond the spatial variation of BMD, this approach has the potential to improve clinical predictions of bone fracture. In addition, FE models facilitate isolating the effect of individual parameters on the distribution of tissue stresses and strains that cannot be measured experimentally. For these reasons, FE methods have been used to determine vertebral strength[10,38,43,44], identify the locations of the vertebrae at high risk for fracture[1,10,43,45-49] and determine the effects of age related changes such as disc degeneration[11,12,21,25-27,50] and osteoporosis.[1,9,11,13,45,51] The FE models developed previously have generally been limited to simulating either physical loading of vertebrae,[10,11,38,43-46,48] or spatial variation of BMD in cancellous bone[11-13,21,25,26,52] and not both. Hence, these models can not accurately assess the fracture risk or locations vulnerable to fracture for physiological loading. In addition, tissue changes in the thoracolumbar junction (T12 to L2) where osteoporotic fractures frequently occur[16,36,53] have not been investigated with a detailed FE model.

The objective of this study was to examine the effect of osteoporotic changes on the mechanics of the L1 vertebra to better understand the factors contributing to fracture. We used a finite element model of the T12-L2 spinal segment with spatially varying bone properties. The FE model was modified to simulate osteoporosis in four stages, which included stiffening of the IVDs and the reduction of the elastic modulus of both cancellous and cortical bone tissue. The solutions for each case were obtained under uniform compression and flexion.

Methods

A detailed FE model of the thoracolumbar junction previously developed and verified (Figure 3.1) was used in this study. The details of the model are explained in Chapter 2. Briefly, computed tomography (CT) images from a 55-year-old female cadaver who had normal bone density and no evident degeneration due to osteoporosis were used to obtain the exact surface geometry of the T12, L1 and L2 vertebrae. The surface models of the vertebrae were converted to 8-noded hexagonal FE meshes (Truegrid, XYZ Scientific Applications, CA). Two IVDs (T12-L1 and L1-L2) composed of an anulus fibrosis and nucleus were modeled between the endplates of the vertebrae. The anulus fibrosis was represented by four layers of stiff fibers embedded in a soft ground material (E=4.2 MPa). [13,54-58] The disc fibers, comprising 19% of the volume of the anulus [54,57,59,60], were oriented in a crisscross pattern making an angle of 30 degrees, on average, with the endplates of the vertebrae [21,22,54,55,57-59] and were modeled with cable elements. The nucleus, comprising about 40% of total IVD volume,[56,57,59] was modeled as a nearly incompressible solid with stiffness of 0.2 MPa [13,61] to represent its gelatinous behavior. Finally, seven structurally relevant ligaments[13,21,22,55,62,63] and facet joints were modeled.

Spatially variable tissue properties were incorporated based on the CT attenuation. An isotropic heterogeneous modulus was assigned to the bone tissue based on an exponential density-elasticity relationship:[64]

$$E = 4730\ \rho^{1.56}$$

where the density (ρ) was obtained from Hounsfield Units (HU). The moduli (E) ranged from 52 to 7970 MPa and the average elastic modulus in the centrum of the

vertebrae varied from 200 to 300 MPa, consistent with the range given for the cancellous bone in the literature.[65-69] Poisson's ratio for the bone tissue was set to 0.3.

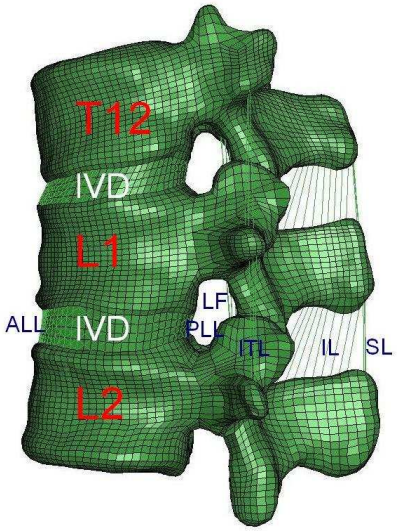

Figure 3.1. Finite element model

Tissue changes due to osteoporosis were simulated in four stages, progressing from disc degeneration to cancellous and cortical bone changes. In stage 1, the elastic modulus of the nucleus was increased to that of the normal anulus ground substance. In stage 2, the elastic modulus of both the nucleus and anulus was doubled to 8.4 MPa.[12] In stage 3, disc degeneration and the stiffness loss of cancellous bone were simulated. For this stage, the elastic modulus of the elements dominating the centrum of the vertebrae (E=52-359 MPa) was reduced by 67%.[10,11,13] In stage 4, in addition to the changes in stage 3, we reduced the elasticity modulus of the elements comprising the vertebral cortex (E=360-680 MPa) by 30%.[13]

Two loading cases were investigated for each case: a uniformly distributed compression (400 N) or a pure flexion moment (7.5 Nm) applied to the superior endplate of T12. The moment was created by applying concentric forces while creating zero axial force. The FE models were restrained in all directions at the inferior endplate of L2. Solutions were obtained using a commercial finite element package (ABAQUS, Hibbitt, Karlsson & Sorensen, Inc, RI).

For each loading case and osteoporotic stage, we calculated axial displacement in compression, and rotation in flexion to obtain the stiffness (or global behavior) of the segment. The largest compressive strain in the vertebral body of L1, the maximum and average principal strains and stresses in the mid-transverse and mid-sagittal cancellous bone sections were determined. The compressive (minimum principal) strains and von Mises stresses were determined at four cortex regions of the mid-transverse section and for the cancellous tissue. The distributions of principal stresses and strains, and von Mises stresses in the mid-transverse and mid-sagittal sections of the L1 vertebra were compared for the normal spine and each successive stage of osteoporosis.

Results

Osteoporotic degeneration of the tissues markedly changed the overall behavior of the segment and the distribution of the high stress and strain regions in the L1 vertebra. Disc degeneration increased the stiffness of the segment but did not bring the strains (or stresses) to the yield point. However, the softening of the bone tissue (especially the cancellous bone) increased the strains closer to the average yield strain (7000

microstrain). We set the upper bound of the compressive strain to 3000 microstrain to measure the volume of tissue at risk for fracture. We determined that 6% and 10% of the vertebral body exceeded the limit after stages 3 and 4, respectively, for compression. About 90% of the high strain regions occurred in the cancellous bone. In flexion, regions at risk for fracture increased further. As in compression, the first two stages (disc degeneration) did not increase the strains to the upper bound. However, high strain regions occupied 16% and 20% of the vertebral body due to the material changes in stages 3 and 4, respectively.

The stiffness of the thoracolumbar spine increased with osteoporotic degeneration of the tissues (Tables 3.1, 3.2). While the stiffness increase in stage 1 was negligible (<8%), the IVD stiffening of stage 2 increased the axial and flexural stiffness by 53% and 32%, respectively. The elastic modulus reductions in the cancellous and cortical bone tissue (stages 3 and 4) slightly reduced (<12%) the stiffness of the segment after stage 2, but still represented ~40% increases over the normal, healthy segment.

The principal stresses and strains changed minimally with the first two stages of osteoporosis. Stiffening of the nucleus (stage 1) had little effect on the stresses and strains in L1. In compression, the largest compressive stress and strain occurred in the posterior cortical wall and slightly decreased with stiffening of the nucleus (Table 3.1). However, in flexion, the stresses and strains in the anterior and posterior cortex increased with nucleus stiffening (Table 3.2). Stiffening of the entire IVD (stage 2) slightly increased the strains compared to the healthy spine (Table 3.1). In

compression, the largest compressive strain in the cortical wall (-2740 με) exceeded that in the healthy segment by only 8%. Although nucleus stiffening reduced stresses and strains in the cancellous bone, stiffening of the entire IVD restored the values to normal or slightly greater (Table 3.3). In flexion, the stress and strain changes in the cortex and cancellous bone were higher than those in compression (Figures 3.6, 3.8 and Tables 3.2, 3.4). The greatest compressive strain change in the mid-transverse cortex was in the posterior cortex (4.1 fold).

The reduction in the elastic modulus of cancellous bone (stage 3) substantially increased the principal strains. In compression, stresses and strains in the cortex of the mid-transverse section increased up to 93% with respect to the normal segment, except in the anterior cortex (Figures 3.2, 3.3 and Table 3.1). The largest compressive stress occurred in the posterior wall and increased by 42% (Table 3.1). Principal strains and stresses in the cancellous bone increased considerably more in the mid-sagittal section (up to 206%) than in the mid-transverse section (up to 160%) (Figures 3.3, 3.7 and Table 3.3). The effects of material changes in stage 3 were more pronounced in flexion than in compression (Figures 3.5, 3.6, 3.8 and Tables 3.2, 3.4). Although the compressive (minimum principal) strain in the mid-transverse posterior cortex was low, its value changed most (6.4 fold). The largest compressive strain occurred in the anterior wall above and below the mid-transverse section. The change in the von Mises stresses in the cancellous bone was either negative or small. However, the principal stresses and strains increased tremendously (up to 3.6 fold) (Figure 3.8 and Table 3.4).

Including cortical changes (stage 4) further increased the principal strains and altered the stresses in the L1. In compression, the compressive strains in the left, right and anterior cortex of mid-transverse section was considerably increased with respect to those in stage 3 (by 27% to 36%) (Table 3.1). The largest compressive strain increased only by 10%. In the cancellous bone, maximum compressive and tensile strains did not change considerably in the mid-transverse section (<3%) or in mid-transverse section (<10%) (Table 3.3). In flexion, von Mises stresses in the left and right mid-transverse cortex slightly (<12%) reduced but strains in all 5 regions increased by at least 23% when compared to those in stage 3 (Table 3.2). The additional changes made in stage 4 did not increase the maximum compressive strain or stress in the vertebral body (<3%). Although the maximum von Mises stress in the cancellous bone reduced (11%), the maximum compressive and tensile strains increased by 6% and 7%, respectively, and occurred in the mid-sagittal section (Table 3.4).

Table 3.1. Axial stiffness of the segment, maximum compressive stress and strain in the cortical bone, von Mises stresses and minimum principal strains at the center, posterior, anterior, left and right cortex of the mid-transverse section of L1 under compression. Stages of osteoporosis: S1 = stiffening of nucleus; S2 = stiffening of nucleus and anulus; S3 = S2 + degradation of cancellous bone; S4 = S3 + degradation of cortical bone

	Normal	S1	S2	S3	S4
Stiffness (kN/mm)	0.77	0.71	1.18	1.11	1.08
Max. stress (MPa)	-1.870	-1.715	-1.810	-2.660	-2.930
Max. Strain (με)	-2540	-2296	-2744	-6249	-6010
Von Mises stresses (MPa)					
center	0.335	0.343	0.336	0.364	0.393
posterior	0.383	0.431	0.503	0.446	0.441
anterior	0.258	0.296	0.271	0.301	0.295
left	0.665	0.668	0.740	0.968	0.915
right	0.467	0.472	0.530	0.752	0.677
Minimum principal strains (με)					
center	-767	-717	-870	-992	-1210
posterior	-1187	-1064	-990	-2288	-2350
anterior	-518	-545	-430	-514	-700
left	-1021	-1037	-1131	-1409	-1745
right	-743	-764	-836	-1120	-1422

Table 3.2. Flexion stiffness of the segment, maximum compressive stress and strain in the cortical bone, von Mises stresses and minimum principal strains at the center, posterior, anterior, left and right cortex of the mid-transverse section of L1 under flexion. Stages of osteoporosis: S1 = stiffening of nucleus; S2 = stiffening of nucleus and anulus; S3 = S2 + degradation of cancellous bone; S4 = S3 + degradation of cortical bone

	Normal	S1	S2	S3	S4
Stiffness (Nm/°)	2.34	2.53	3.10	2.87	2.73
Max. stress (MPa)	-2.400	-2.100	-2.230	-2.150	-2.210
Max. Strain (με)	-2940	-2131	-2723	-7710	-7778
Von Mises stresses (MPa)					
center	0.181	0.142	0.146	0.142	0.133
posterior	0.092	0.19	0.327	0.265	0.208
anterior	0.472	0.547	0.749	0.803	0.829
left	0.338	0.327	0.314	0.360	0.340
right	0.178	0.181	0.191	0.223	0.195
Minimum principal strains (με)					
center	-429	-312	-320	-338	-580
posterior	-58	-125	-240	-373	-430
anterior	-953	-1006	-1280	-1456	-1880
left	-566	-552	-533	-607	-746
right	-313	-321	-333	-389	-490

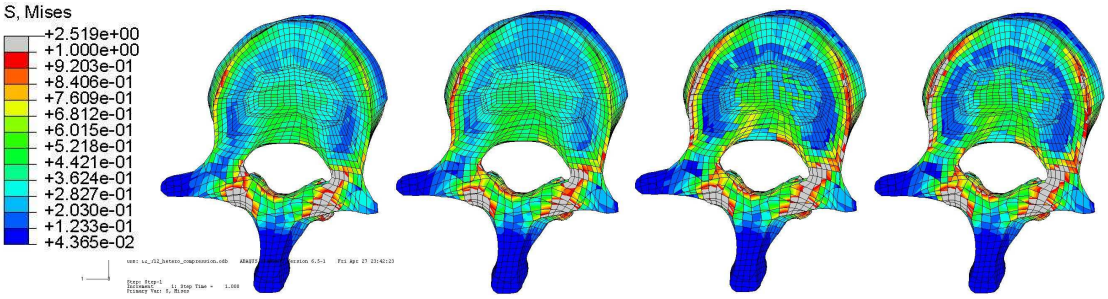

Figure 3.2. von Mises stresses (in MPa) in the mid-transverse section due to compression

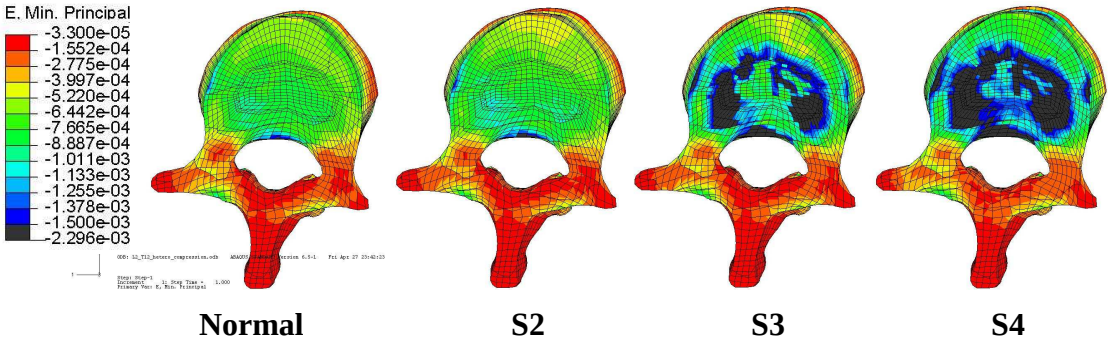

Figure 3.3. Minimum principal strains (in microstrains) in the mid-transverse section due to compression

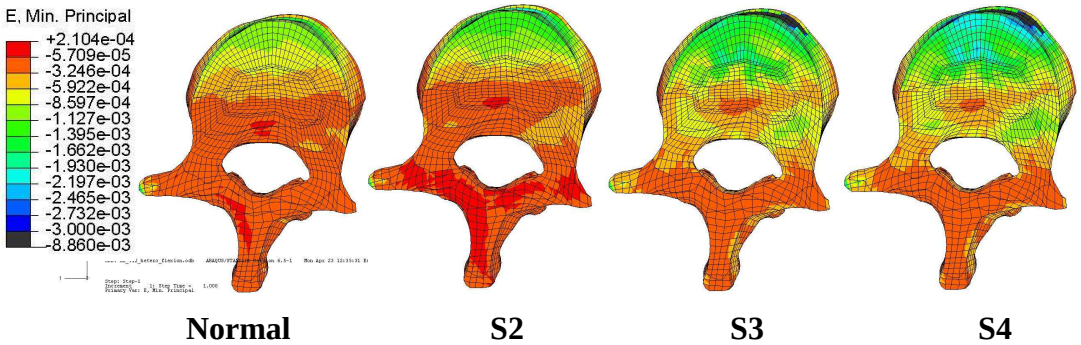

Figure 3.4. Minimum principal strains (in microstrains) in the mid-transverse section due to flexion

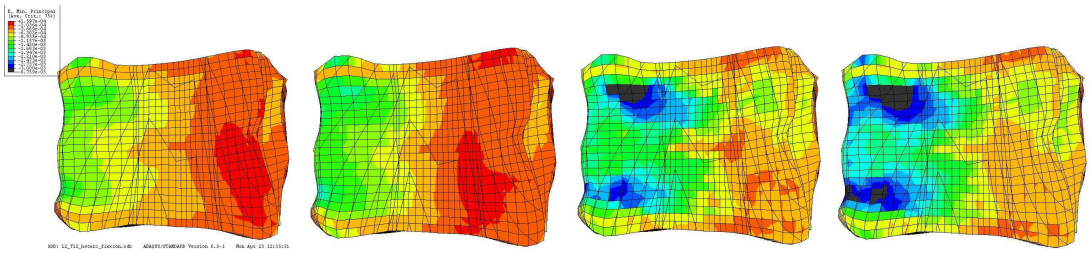

Figure 3.5. Minimum principal strains (in microstrains) in the mid-sagittal section due to flexion

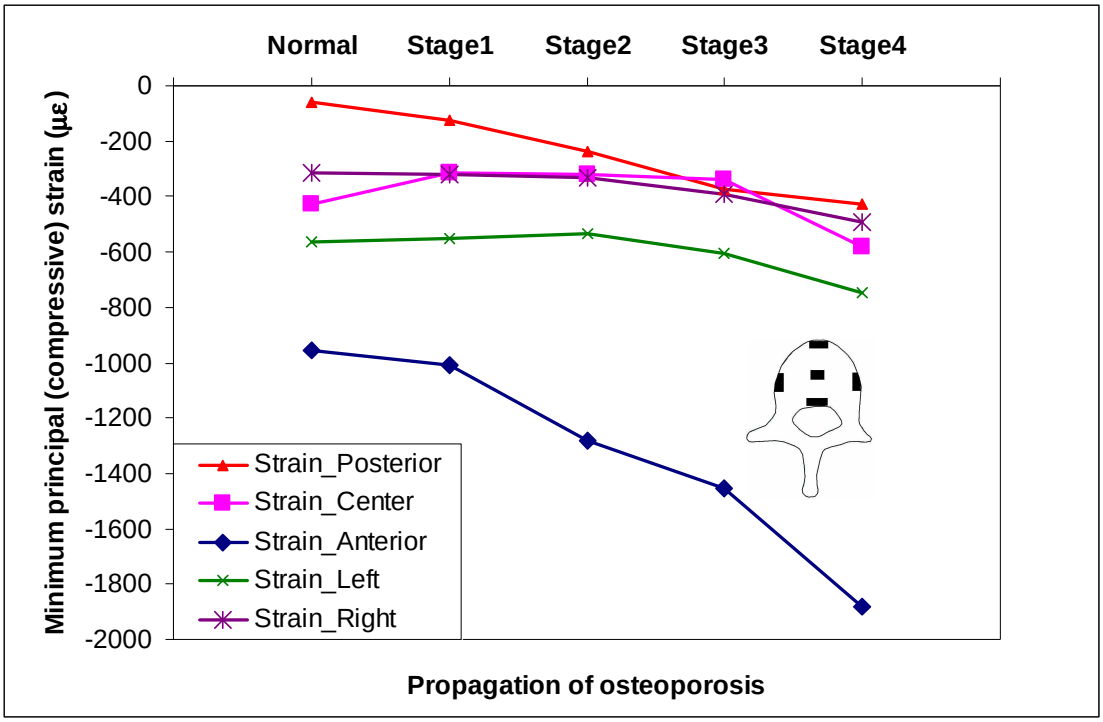

Figure 3.6. Compressive (minimum principal) strains in 5 regions of the mid-transverse section with the progression of osteoporosis under flexion

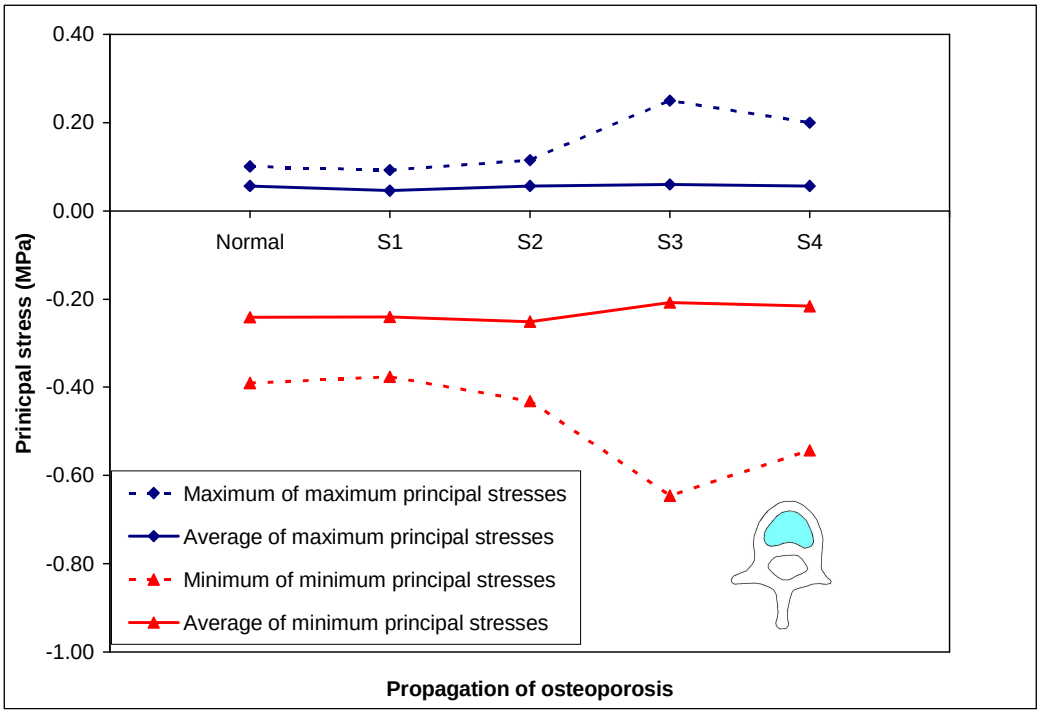

Figure 3.7. Principal stresses in the mid-transverse cancellous bone with the progression of osteoporosis under compression

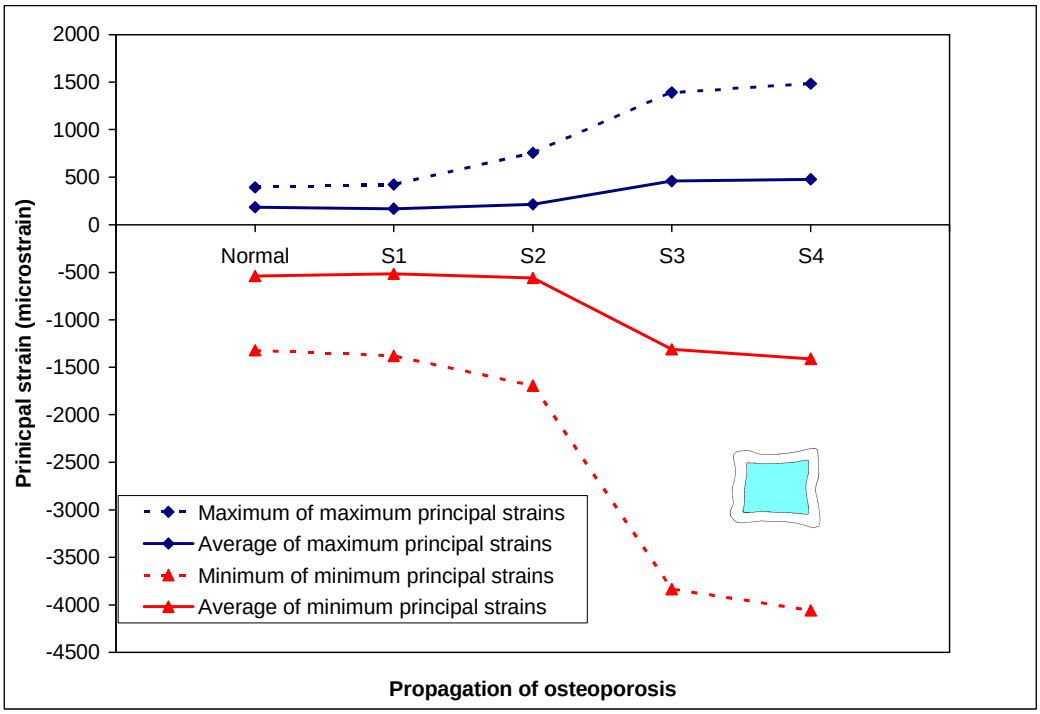

Figure 3.8. Principal strains in the mid-sagittal cancellous bone with the progression of osteoporosis under flexion

Table 3.3. Minimum, maximum and average principal stresses and strains in the cancellous bone in the mid-transverse (MT) and mid-sagittal (MS) sections of L1 under compression. Stages of osteoporosis: S1 = stiffening of nucleus; S2 = stiffening of nucleus and anulus; S3 = S2 + degradation of cancellous bone; S4 = S3 + degradation of cortical bone

			Normal	Stages of Osteoporosis			
				S1	S2	S3	S4
Max principal strain	maximum (με)	MT	468	434	540	1044	1145
		MS	531	405	436	1074	1068
	mean (με)	MT	298	272	311	628	694
		MS	320	271	287	617	663
Min principal strain	maximum (με)	MT	-952	-910	-994	-2476	-2598
		MS	-1344	-1223	-1344	-4116	-4004
	mean (με)	MT	-735	-724	-762	-1441	-1641
		MS	-930	-865	-896	-2098	-2243
Max principal stress	maximum (MPa)	MT	0.10	0.09	0.12	0.25	0.20
		MS	0.15	0.09	0.10	0.19	0.14
	mean (MPa)	MT	0.06	0.05	0.06	0.06	0.06
		MS	0.05	0.04	0.04	0.03	0.03
Min principal stress	maximum (MPa)	MT	-0.39	-0.38	-0.43	-0.65	-0.54
		MS	-0.43	-0.40	-0.47	-0.97	-0.75
	mean (MPa)	MT	-0.24	-0.24	-0.25	-0.21	-0.22
		MS	-0.30	-0.28	-0.29	-0.27	-0.27
von Mises stress	maximum (MPa)	MT	0.47	0.44	0.50	0.71	0.60
		MS	0.49	0.45	0.52	0.94	0.74
	mean (MPa)	MT	0.28	0.27	0.29	0.25	0.25
		MS	0.34	0.31	0.32	0.29	0.29

Table 3.4. Minimum, maximum and average principal stresses and strains in the cancellous bone in the mid-transverse (MT) and mid-sagittal (MS) sections of L1 under flexion. Stages of osteoporosis: S1 = stiffening of nucleus; S2 = stiffening of nucleus and anulus; S3 = S2 + degradation of cancellous bone; S4 = S3 + degradation of cortical bone

			Normal	Stage of Osteoporosis			
				S1	S2	S3	S4
Max principal strain	maximum (με)	MT	249	255	357	754	748
		MS	392	425	755	1392	1486
	mean (με)	MT	135	121	144	310	343
		MS	185	168	215	458	480
Min principal strain	maximum (με)	MT	-910	-957	-1182	-2007	-2200
		MS	-1321	-1380	-1695	-3833	-4057
	mean (με)	MT	-417	-413	-448	-791	-922
		MS	-540	-518	-560	-1312	-1411
Max principal stress	maximum (MPa)	MT	0.04	0.05	0.13	0.17	0.12
		MS	0.12	0.13	0.23	0.18	0.16
	mean (MPa)	MT	0.02	0.01	0.02	0.02	0.02
		MS	0.03	0.02	0.04	0.03	0.03
Min principal stress	maximum (MPa)	MT	-0.41	-0.43	-0.53	-0.50	-0.52
		MS	-0.47	-0.49	-0.60	-0.57	-0.55
	mean (MPa)	MT	-0.14	-0.14	-0.15	-0.12	-0.13
		MS	-0.17	-0.17	-0.18	-0.16	-0.17
von Mises stress	maximum (MPa)	MT	0.43	0.45	0.55	0.61	0.59
		MS	0.49	0.51	0.62	0.64	0.57
	mean (MPa)	MT	0.15	0.15	0.16	0.13	0.14
		MS	0.19	0.18	0.21	0.18	0.18

Discussion

In this study, we investigated the progressive effects of tissue changes due to osteoporosis on the overall behavior of the thoracolumbar spinal segment where vertebral fractures often occur.[16,36,53] We report the stress and strain predictions for the L1 vertebra since the physical boundaries of L1 were completely modeled. While the stiffened discs mainly reduced the flexibility of the overall segment and not tissue strains, the material changes in the bone tissue substantially increased the fracture risk of the segment by increasing not only the principal strains but also volume of bone tissue subjected to high strains. High strains occurred mainly in the cancellous bone (just below the superior endplate), suggesting that fracture initiates in the cancellous bone with the knowledge that the yield strain of both cancellous and cortical tissues are almost the same.[70] Use of heterogeneous bone properties enable us to accurately map the distribution of strain throughout the vertebra.

Increased stiffness of the spine with restrained motions may cause pain and degeneration of vertebrae, which is an important health issue. As we observed, disc degeneration defined in our study significantly increased both axial and flexion stiffness of the segment verifying previously reported results.[21,28,30] In addition, disc degeneration altered the loading of the superior endplate of L1 thereby changing the distributions of stresses and strains in L1 (Figures 3.2-3.5), in agreement with previous studies.[11,21,25,28,30,50] Our results do not support the general statement that disc degeneration increases the stresses in the cortical bone.[25,28] Although we observed the same results throughout the vertebra, at some locations stresses reduced depending on

the loading mode, which is in agreement with prior experimental data.[50] We believe the heterogeneous material properties of the vertebrae used in our study contributed to this difference. In the same context, in compression, the anterior strains decreased, implying that disc degeneration relieves the anterior side, and in flexion, the rate of strain increase in the anterior was greater than that in other locations (Figure 3.6), meaning that the risk of anterior wedge fracture increases, and that disc degeneration altered load sharing, which are in agreement with previous findings.[50] Our results do not demonstrate that disc degeneration reduced the stresses in the cancellous bone.[45] Although we obtained the same result for the mid-transverse section subjected to compression, the cancellous bone stresses in flexion increased with disc degeneration. The reason for the difference in the predictions may be the use of isolated vertebral bodies by Homminga et al.[45]

Like disc degeneration, the reduction in the elastic modulus of bone tissue changed the global behavior of the segment i.e., reduced stiffness of bone tissue reduced the axial and flexion stiffness of the segment, verifying the previously published results.[13] However, the changes in the stresses and strains due to the reduction in the elastic modulus of the bone tissues were more pronounced than the stiffness decrease of the segment. From stage 2 to stage 3 compressive strains in the cortex of the mid-transverse section increased, in agreement with other studies.[1,9,11,45] However, the effect in the cancellous bone was more significant since the area of the high strain elements (shown in gray in Figures 3.3, 3.5) increased markedly in the centrum of the vertebral body after stage 3 as reported previously.[45] Although, osteoporosis

significantly increased the cancellous tissue subjected to higher strains, the volume of bone tissue subjected to high von Mises stresses changed minimally (Figure 3.2), reflecting the finding that bone tissue failure is dependent on the applied strain level.[46,48,49] We also observed that in the cancellous bone, maximum compressive strain was always higher than the maximum tensile strain (2.3-3.8 fold), and maximum compressive stress was higher that maximum tensile stress (2.6-5.3 fold) which suggest that the fracture of the vertebrae will initiate in compression for both loading modes investigated. The reduction in the elastic modulus of the cortical bone (stage 4) changed the stresses and strains but to a lesser extent than the reduction of the elastic modulus of cancellous bone did.

Softening of cortical tissue, increased the stresses and strains in both the cortical and cancellous bone, demonstrating that deterioration of a single tissue envelope causes redistribution of stresses throughout the vertebra.

The loading mode of the spine substantially contributed to the mechanism of vertebral fracture. When the segment is loaded in flexion, the high compressive strain regions (shown in gray in Figure 3.5) occurred just below the superior and above the inferior endplates of the anterior vertebra, producing an increased risk for anterior wedge fractures. This result is in agreement with clinical findings that that the anterior wedge fracture is the most frequently observed fracture type.[36,71-73]

Our study contains several strengths compared to prior work. We incorporated heterogeneous bone properties and physical boundary conditions for the analysis of the progression of osteoporosis in the L1 vertebra, which facilitates the determination of an accurate stress distribution on the endplates and in the L1 vertebra to better assess fracture risk. In terms of capturing the complete physical boundary conditions of L1, our model is an improvement over two vertebra spinal segments.[12,13,22,54,55,58] We incorporated patient specific, vertebral geometry and material properties, without any assumptions of symmetry, average geometry and flat endplates, which would underestimate stresses and strains and change the load paths. In addition, our model better captured the true geometry than isolated vertebral models developed from CT scans that use voxel-based elements causing a loss in the accuracy of the true geometry and the cortical shell.[10,38,45,74] However, our model development is not as automated as in the voxel-based approach. Finally, we evaluated not only the effects of disc degeneration but also those of bone loss, which allowed us to simulate the effects of progressive tissue degeneration.

Our models have several limitations. We did not include viscosity, porosity and nonlinearity of the materials. Therefore, impact or time dependent loading can not be simulated. Due to these simplifications, we also can not capture the full mechanical behavior of the motion segment. Bone tissue is not isotropic[17,75-77] and we excluded the orthotropic (or transversely isotropic) behavior of the bone tissue in our model, which may underestimate the transverse stresses and strains. We neglected the

presence of musculature in our model. Finally, our conclusions are based on a data from a single individual.

A better understanding of areas of vulnerability under physiological loading will provide insights into failure locations and improve efforts towards reconstruction after fracture and fixation of osteoporotic vertebral bodies. This model clearly delineates that osteoporotic bone is at high risk for fracture through not only increased bone stresses and strains, but also changes in the volume and location of bone experiencing these high strains. In addition, this study clearly shows that disc degeneration relieves stresses at some locations and increases stresses at other locations depending on the loading mode. In this study, we focused on the L1 vertebra but the stresses and strains in neighboring vertebrae (as well as L1) will also change with treatment methods such as vertebroplasty, kyphoplasty, spinal fusion or disc replacement. To truly understand the effects of such treatments on the treated vertebra and neighboring vertebrae, FE models need to incorporate at least four vertebrae with patient specific material properties and physical loading conditions.

REFERENCES

1. Homminga J, Van-Rietbergen B, Lochmuller EM, et al. The osteoporotic vertebral structure is well adapted to the loads of daily life, but not to infrequent "error" loads. Bone 2004;34:510-6.
2. Myers ER, Wilson SE. Biomechanics of osteoporosis and vertebral fracture. Spine 1997;22:25S-31S.
3. Lane JM, Russell L, Khan SN. Osteoporosis. Clin Orthop Relat Res 2000:139-50.
4. Lane JM, Serota AC, Raphael B. Osteoporosis: differences and similarities in male and female patients. Orthop Clin North Am 2006;37:601-9.
5. Riggs BL, Melton LJ, 3rd. The worldwide problem of osteoporosis: insights afforded by epidemiology. Bone 1995;17:505S-511S.
6. Sambrook P, Cooper C. Osteoporosis. Lancet 2006;367:2010-8.
7. Guo XE, Kim CH. Mechanical consequence of trabecular bone loss and its treatment: a three-dimensional model simulation. Bone 2002;30:404-11.
8. Werner HJ, Martin H, Behrend D, et al. The loss of stiffness as osteoporosis progresses. Med Eng Phys 1996;18:601-6.
9. Mizrahi J, Silva MJ, Keaveny TM, et al. Finite-element stress analysis of the normal and osteoporotic lumbar vertebral body. Spine 1993;18:2088-96.
10. Faulkner KG, Cann CE, Hasegawa BH. Effect of bone distribution on vertebral strength: assessment with patient-specific nonlinear finite element analysis. Radiology 1991;179:669-74.
11. Villarraga ML, Bellezza AJ, Harrigan TP, et al. The biomechanical effects of kyphoplasty on treated and adjacent nontreated vertebral bodies. J Spinal Disord Tech 2005;18:84-91.
12. Natarajan RN, Chen BH, An HS, et al. Anterior cervical fusion: a finite element model study on motion segment stability including the effect of osteoporosis. Spine 2000;25:955-61.
13. Polikeit A, Nolte LP, Ferguson SJ. The effect of cement augmentation on the load transfer in an osteoporotic functional spinal unit: finite-element analysis. Spine 2003;28:991-6.
14. Keyak JH, Rossi SA. Prediction of femoral fracture load using finite element models: an examination of stress- and strain-based failure theories. J Biomech 2000;33:209-14.
15. Heini PF, Berlemann U, Kaufmann M, et al. Augmentation of mechanical properties in osteoporotic vertebral bones--a biomechanical investigation of

vertebroplasty efficacy with different bone cements. Eur Spine J 2001;10:164-71.

16. Melton LJ, 3rd, Wahner HW. Defining osteoporosis. Calcif Tissue Int 1989;45:263-4.

17. Burstein AH, Reilly DT, Martens M. Aging of bone tissue: mechanical properties. J Bone Joint Surg Am 1976;58:82-6.

18. Dickenson RP, Hutton WC, Stott JR. The mechanical properties of bone in osteoporosis. J Bone Joint Surg Br 1981;63-B:233-8.

19. Ritzel H, Amling M, Posl M, et al. The thickness of human vertebral cortical bone and its changes in aging and osteoporosis: a histomorphometric analysis of the complete spinal column from thirty-seven autopsy specimens. J Bone Miner Res 1997;12:89-95.

20. Margulies JY, Payzer A, Nyska M, et al. The relationship between degenerative changes and osteoporosis in the lumbar spine. Clin Orthop Relat Res 1996:145-52.

21. Kim YE, Goel VK, Weinstein JN, et al. Effect of disc degeneration at one level on the adjacent level in axial mode. Spine 1991;16:331-5.

22. Goel VK, Monroe BT, Gilbertson LG, et al. Interlaminar shear stresses and laminae separation in a disc. Finite element analysis of the L3-L4 motion segment subjected to axial compressive loads. Spine 1995;20:689-98.

23. Buckwalter JA. Aging and degeneration of the human intervertebral disc. Spine 1995;20:1307-14.

24. Adams MA, Roughley PJ. What is intervertebral disc degeneration, and what causes it? Spine 2006;31:2151-61.

25. Kurowski P, Kubo A. The relationship of degeneration of the intervertebral disc to mechanical loading conditions on lumbar vertebrae. Spine 1986;11:726-31.

26. Natarajan RN, Williams JR, Andersson GB. Recent advances in analytical modeling of lumbar disc degeneration. Spine 2004;29:2733-41.

27. Pollintine P, Dolan P, Tobias JH, et al. Intervertebral disc degeneration can lead to "stress-shielding" of the anterior vertebral body: a cause of osteoporotic vertebral fracture? Spine 2004;29:774-82.

28. Kumaresan S, Yoganandan N, Pintar FA, et al. Contribution of disc degeneration to osteophyte formation in the cervical spine: a biomechanical investigation. J Orthop Res 2001;19:977-84.

29. Iatridis JC, Setton LA, Weidenbaum M, et al. Alterations in the mechanical behavior of the human lumbar nucleus pulposus with degeneration and aging. J Orthop Res 1997;15:318-22.

30. Shirazi-Adl A. Finite-element simulation of changes in the fluid content of human lumbar discs. Mechanical and clinical implications. Spine 1992;17:206-12.

31. Oleksik A, Lips P, Dawson A, et al. Health-related quality of life in postmenopausal women with low BMD with or without prevalent vertebral fractures. J Bone Miner Res 2000;15:1384-92.

32. Gold DT. The clinical impact of vertebral fractures: quality of life in women with osteoporosis. Bone 1996;18:185S-189S.

33. Tosteson AN, Hammond CS. Quality-of-life assessment in osteoporosis: health-status and preference-based measures. Pharmacoeconomics 2002;20:289-303.

34. U.S. Department of Health and Human Services. Health and Osteoporosis: A Report of the Surgeon General. Rockville, MD: Department of Health and Human Services, Office of the Surgeon General; 2004

35. Gustafsson L, Jacobson B, Kusoffsky L. X ray spectrophotometry for bone-mineral determinations. Med Biol Eng 1974;12:113-9.

36. Melton LJ, 3rd, Kan SH, Frye MA, et al. Epidemiology of vertebral fractures in women. Am J Epidemiol 1989;129:1000-11.

37. Cauley JA, Zmuda JM, Wisniewski SR, et al. Bone mineral density and prevalent vertebral fractures in men and women. Osteoporos Int 2004;15:32-7.

38. Crawford RP, Cann CE, Keaveny TM. Finite element models predict in vitro vertebral body compressive strength better than quantitative computed tomography. Bone 2003;33:744-50.

39. Kanis JA, Borgstrom F, De Laet C, et al. Assessment of fracture risk. Osteoporos Int 2005;16:581-9.

40. Schuit SC, van der Klift M, Weel AE, et al. Fracture incidence and association with bone mineral density in elderly men and women: the Rotterdam Study. Bone 2004;34:195-202.

41. Lafferty FW, Rowland DY. Correlations of dual-energy X-ray absorptiometry, quantitative computed tomography, and single photon absorptiometry with spinal and non-spinal fractures. Osteoporos Int 1996;6:407-15.

42. Grampp S, Genant HK, Mathur A, et al. Comparisons of noninvasive bone mineral measurements in assessing age-related loss, fracture discrimination, and diagnostic classification. J Bone Miner Res 1997;12:697-711.

43. Liebschner MA, Kopperdahl DL, Rosenberg WS, et al. Finite element modeling of the human thoracolumbar spine. Spine 2003;28:559-65.

44. Buckley JM, Loo K, Motherway J. Comparison of quantitative computed tomography-based measures in predicting vertebral compressive strength. Bone 2007;40:767-74.

45. Homminga J, Weinans H, Gowin W, et al. Osteoporosis changes the amount of vertebral trabecular bone at risk of fracture but not the vertebral load distribution. Spine 2001;26:1555-61.

46. Silva MJ, Keaveny TM, Hayes WC. Computed tomography-based finite element analysis predicts failure loads and fracture patterns for vertebral sections. J Orthop Res 1998;16:300-8.

47. Kosmopoulos V, Keller TS. Finite element modeling of trabecular bone damage. Comput Methods Biomech Biomed Engin 2003;6:209-16.

48. Kopperdahl DL, Roberts AD, Keaveny TM. Localized damage in vertebral bone is most detrimental in regions of high strain energy density. J Biomech Eng 1999;121:622-8.

49. Kopperdahl DL, Pearlman JL, Keaveny TM. Biomechanical consequences of an isolated overload on the human vertebral body. J Orthop Res 2000;18:685-90.

50. Adams MA, Pollintine P, Tobias JH, et al. Intervertebral disc degeneration can predispose to anterior vertebral fractures in the thoracolumbar spine. J Bone Miner Res 2006;21:1409-16.

51. Keaveny TM, Donley DW, Hoffmann PF, et al. Effects of teriparatide and alendronate on vertebral strength as assessed by finite element modeling of QCT scans in women with osteoporosis. J Bone Miner Res 2007;22:149-57.

52. Noailly J, Lacroix D, Planell JA. Finite element study of a novel intervertebral disc substitute. Spine 2005;30:2257-64.

53. Cooper C, Atkinson EJ, O'Fallon WM, et al. Incidence of clinically diagnosed vertebral fractures: a population-based study in Rochester, Minnesota, 1985-1989. J Bone Miner Res 1992;7:221-7.

54. Natarajan RN, Andersson GB. The influence of lumbar disc height and cross-sectional area on the mechanical response of the disc to physiologic loading. Spine 1999;24:1873-81.

55. Shirazi-Adl A, Ahmed AM, Shrivastava SC. A finite element study of a lumbar motion segment subjected to pure sagittal plane moments. J Biomech 1986;19:331-50.

56. Chen CS, Cheng CK, Liu CL, et al. Stress analysis of the disc adjacent to interbody fusion in lumbar spine. Med Eng Phys 2001;23:483-91.

57. Guo LX, Teo EC, Lee KK, et al. Vibration characteristics of the human spine under axial cyclic loads: effect of frequency and damping. Spine 2005;30:631-7.

58. Qiu TX, Tan KW, Lee VS, et al. Investigation of thoracolumbar T12-L1 burst fracture mechanism using finite element method. Med Eng Phys 2006;28:656-64.

59. White A, Panjabi M. Biomechanics of the Spine. Philadelphia: JB Lippincott; 1990.

60. Broberg KB. On the mechanical behaviour of intervertebral discs. Spine 1983;8:151-65.

61. Sharma M, Langrana NA, Rodriguez J. Role of ligaments and facets in lumbar spinal stability. Spine 1995;20:887-900.

62. Pintar FA, Yoganandan N, Myers T, et al. Biomechanical properties of human lumbar spine ligaments. J Biomech 1992;25:1351-6.

63. Chazal J, Tanguy A, Bourges M, et al. Biomechanical properties of spinal ligaments and a histological study of the supraspinal ligament in traction. J Biomech 1985;18:167-76.

64. Morgan EF, Bayraktar HH, Keaveny TM. Trabecular bone modulus-density relationships depend on anatomic site. J Biomech 2003;36:897-904.

65. Morgan EF, Keaveny TM. Dependence of yield strain of human trabecular bone on anatomic site. J Biomech 2001;34:569-77.

66. Uchiyama T, Tanizawa T, Muramatsu H, et al. Three-dimensional microstructural analysis of human trabecular bone in relation to its mechanical properties. Bone 1999;25:487-91.

67. van Lenthe GH, Stauber M, Muller R. Specimen-specific beam models for fast and accurate prediction of human trabecular bone mechanical properties. Bone 2006;39:1182-9.

68. Kopperdahl DL, Keaveny TM. Yield strain behavior of trabecular bone. J Biomech 1998;31:601-8.

69. Cendre E, Mitton D, Roux JP, et al. High-resolution computed tomography for architectural characterization of human lumbar cancellous bone: relationships with histomorphometry and biomechanics. Osteoporos Int 1999;10:353-60.

70. Morgan EF, Keaveny TM. Dependence of yield strain of human trabecular bone on anatomic site. J Biomech 2001;34:569-77.

71. Melton LJ, 3rd, Lane AW, Cooper C, et al. Prevalence and incidence of vertebral deformities. Osteoporos Int 1993;3:113-9.

72. Eastell R, Cedel SL, Wahner HW, et al. Classification of vertebral fractures. J Bone Miner Res 1991;6:207-15.

73. Rehman Q, Lang T, Modin G, et al. Quantitative computed tomography of the lumbar spine, not dual x-ray absorptiometry, is an independent predictor of prevalent vertebral fractures in postmenopausal women with osteopenia receiving long-term glucocorticoid and hormone-replacement therapy. Arthritis Rheum 2002;46:1292-7.

74. Crawford RP, Keaveny TM. Relationship between axial and bending behaviors of the human thoracolumbar vertebra. Spine 2004;29:2248-55.

75. Mosekilde L, Danielsen CC. Biomechanical competence of vertebral trabecular bone in relation to ash density and age in normal individuals. Bone 1987;8:79-85.

76. Ulrich D, van Rietbergen B, Laib A, et al. The ability of three-dimensional structural indices to reflect mechanical aspects of trabecular bone. Bone 1999;25:55-60.

77. Galante J, Rostoker W, Ray RD. Physical properties of trabecular bone. Calcif Tissue Res 1970;5:236-46.

APPENDICES

DATA FOR EVALUATION OF SLENDER GRAPHITE RODS

Finite element model of the graphite rod (finer mesh)

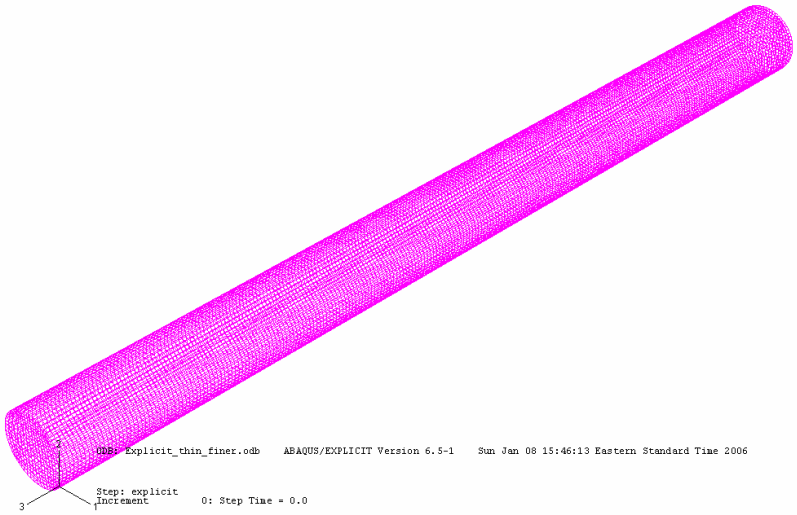

Frequency content of the rod obtained from coarse and fine meshes

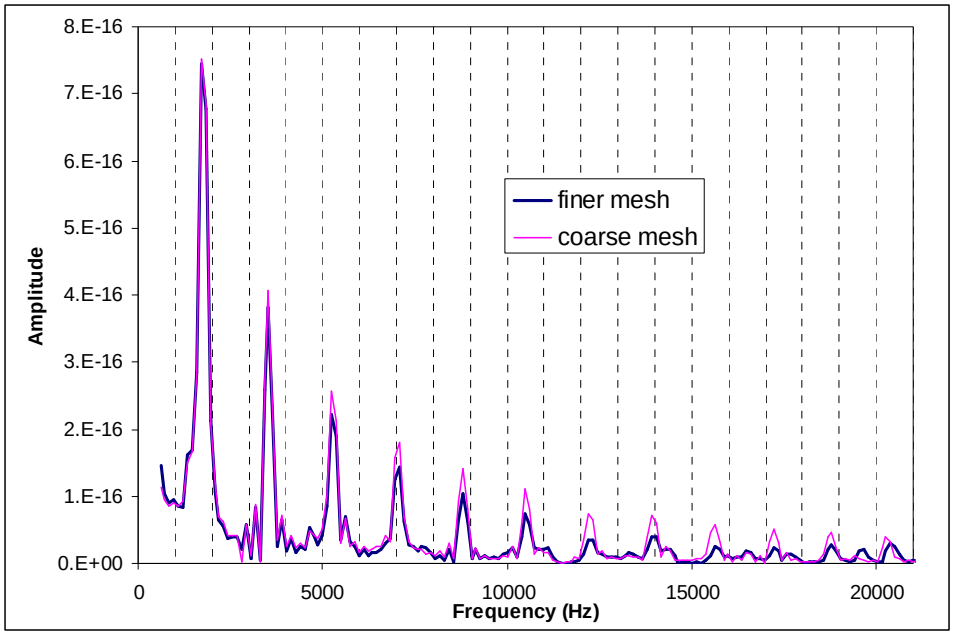

Frequency content of the rod obtained for different analysis time

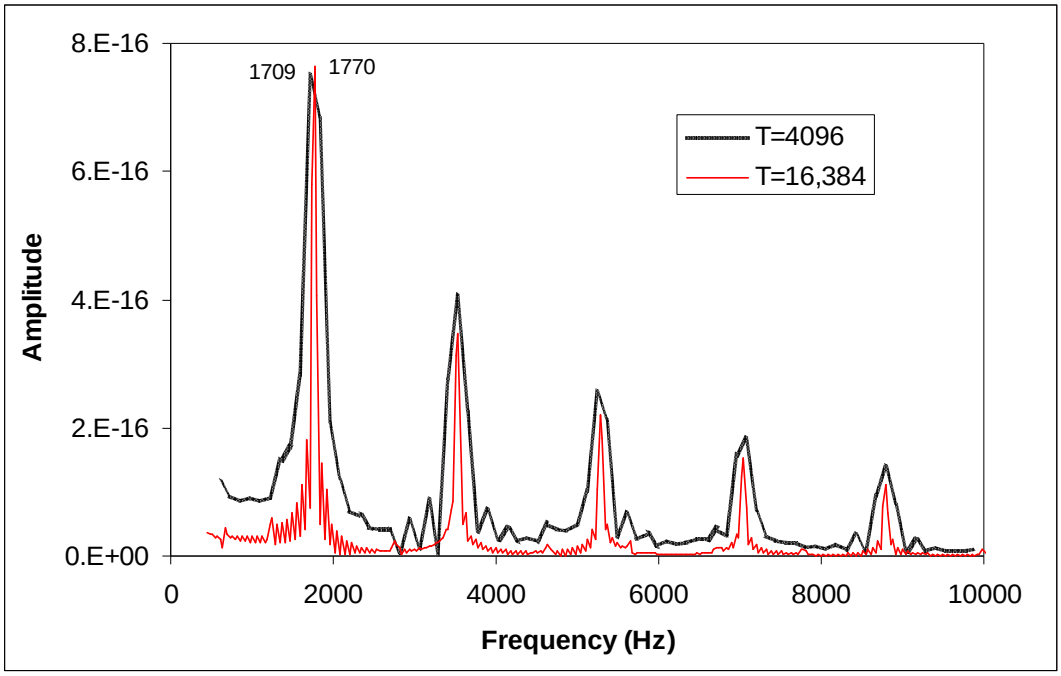

Frequency content of ROD 7 (un-cracked, reference specimen) obtained by impact-echo test

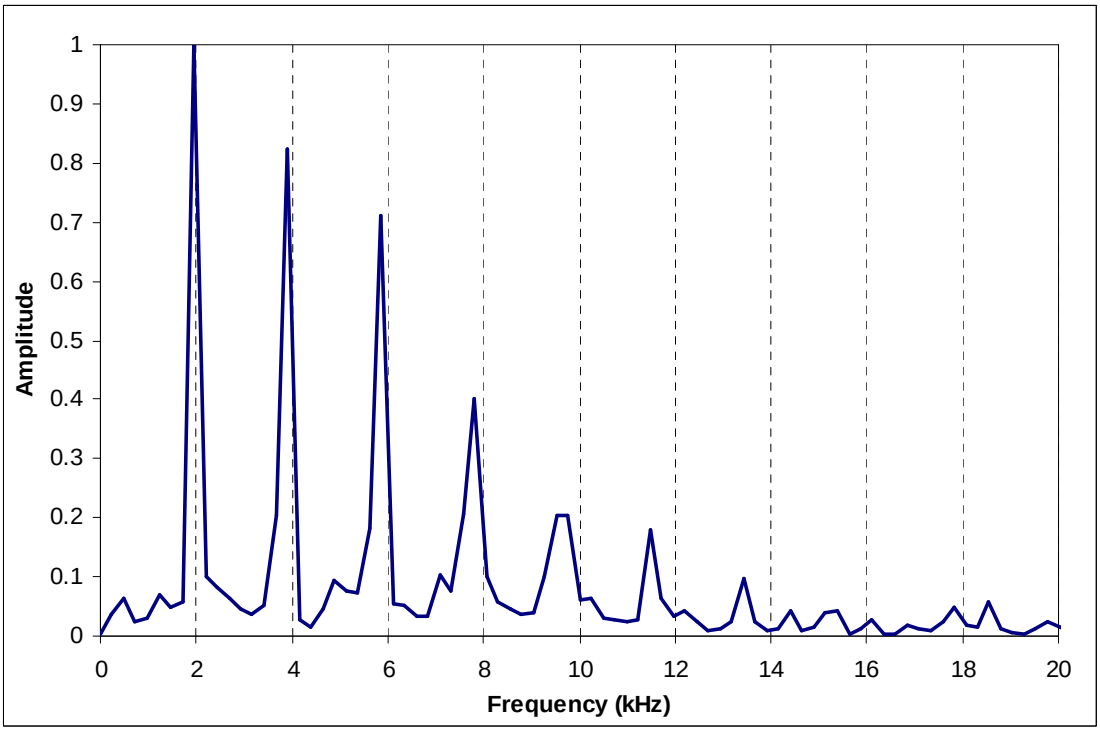

MESH SIZE ANALYSIS OF VERTEBRAL BODY

Finite element model of the L1 vertebral body (coarse and fine meshes)

Two different mesh sizes were used in the L1 vertebral body. For the coarse mesh, 8-node or 20-node hexagonal elements were used. For the fine mesh, only 20-node hexagonal elements were used. Both meshes performed well. Fine mesh was used throughout this study. Results are summarized below.

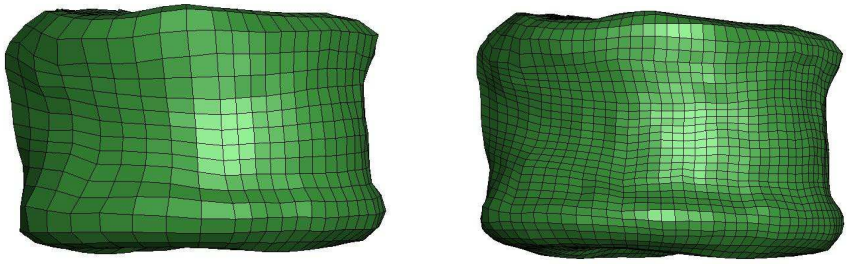

LOAD	Output	Coarse 8 node	Coarse 20 node	Fine 8 node
Compression	Superior posterior displacement (mm)	2.12	2.13	2.14
	Superior central displacement (mm)	2.30	2.32	2.29
	Anterior mid-transverse von Mises stress (MPa)	92.56	92.2	92.21
	Superior left minimum principal strain	-0.09170	-0.08310	-0.09357
	Superior left von Mises sress (MPa)	79.60	69.83	82.52
	Superior posterior-left minimum principal strain	-0.11046	-0.09970	-0.10830
	Superior central von Mises stress (MPa)	59.94	60.27	56.66
Flexion	Superior posterior displacement (mm)	0.135	0.137	0.135
	Superior central displacement (mm)	0.076	0.076	0.079
	Anterior mid-transverse von Mises stress (MPa)	4.32	4.22	4.28
	Superior anterior minimum principal strain	-0.00487	-0.00452	-0.00467
	Superior anterior von Mises (MPa)	4.23	3.79	4.30
	Superior posterior-left maximum principal strain	0.00505	0.00481	0.00498

COMPARISON BETWEEN 3 VERTEBRAE AND 4 VERTEBRAE SPINAL SEGMENTS

Finite element model of T11-L2 spinal segment

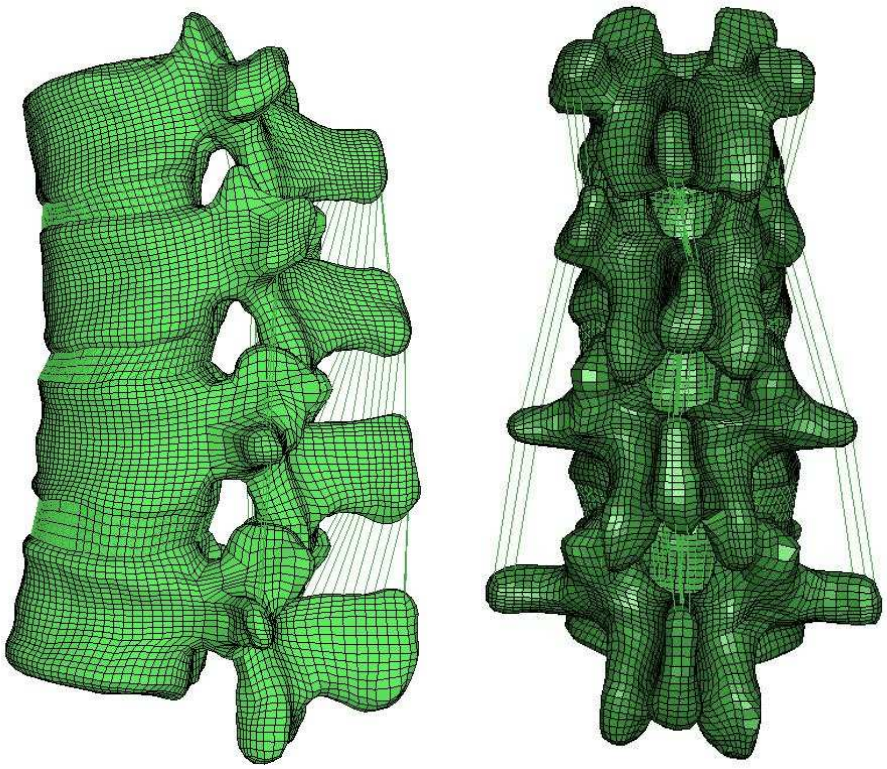

3 VERTEBRAE (T12-L2) **4 VERTEBRAE (T11-L2)**

Von Mises Stresses for Compression

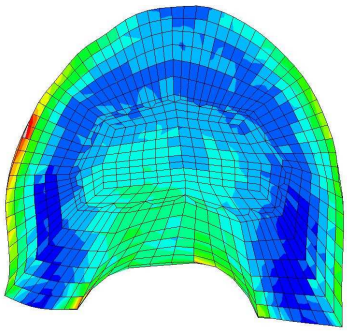

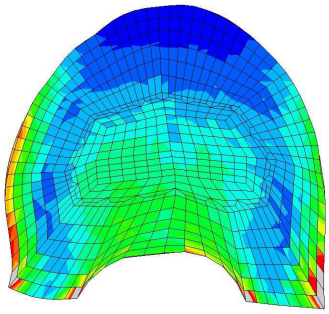

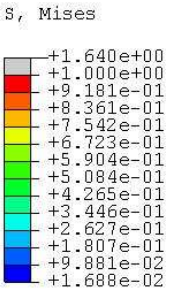

Von Mises Stresses for Flexion

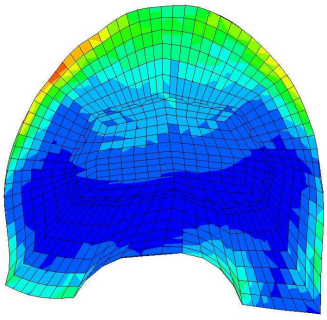

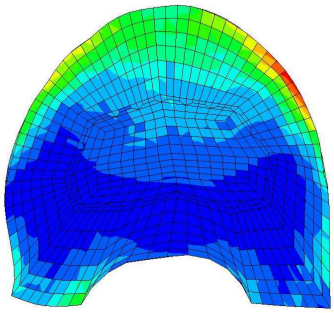

Minimum Principal Strains for Compression

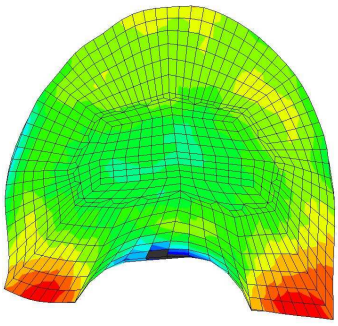

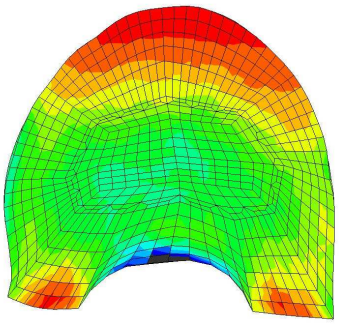

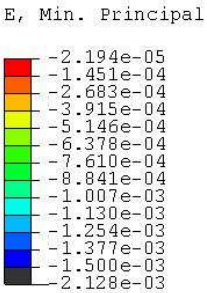

Minimum Principal Strains for Flexion

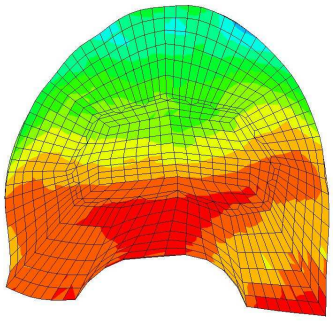

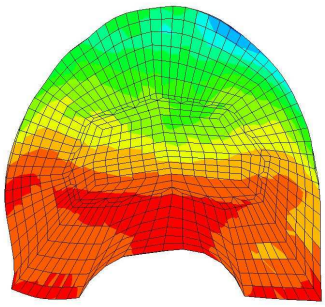

		T12-L2	T11-L2	Δ (%)
Compression	Von Mises, posterior (MPa)	0.383	0.414	-8
	Von Mises, center (MPa)	0.335	0.33	1
	Von Mises, anterior (MPa)	0.258	0.035	86
	Von Mises, left (MPa)	0.665	0.645	3
	Von Mises, right (MPa)	0.467	0.42	10
	Min principal strain, posterior (-micro)	1187	1305	-10
	Min principal strain, center (-micro)	767	924	-20
	Min principal strain, anterior (-micro)	518	71	86
	Min principal strain, left (-micro)	1021	813	20
	Min principal strain, right (-micro)	743	614	17
Flexion	Von Mises, posterior (MPa)	0.092	0.08	13
	Von Mises, center (MPa)	0.181	0.158	13
	Von Mises, anterior (MPa)	0.472	0.423	10
	Von Mises, left (MPa)	0.338	0.131	61
	Von Mises, right (MPa)	0.178	0.291	-63
	Min principal strain, posterior (-micro)	58	49	16
	Min principal strain, center (-micro)	429	452	-5
	Min principal strain, anterior (-micro)	953	910	5
	Min principal strain, left (-micro)	566	200	65
	Min principal strain, right (-micro)	313	548	-75

EFFECT OF NONLINEAR PROPERTIES OF LIGAMENTS

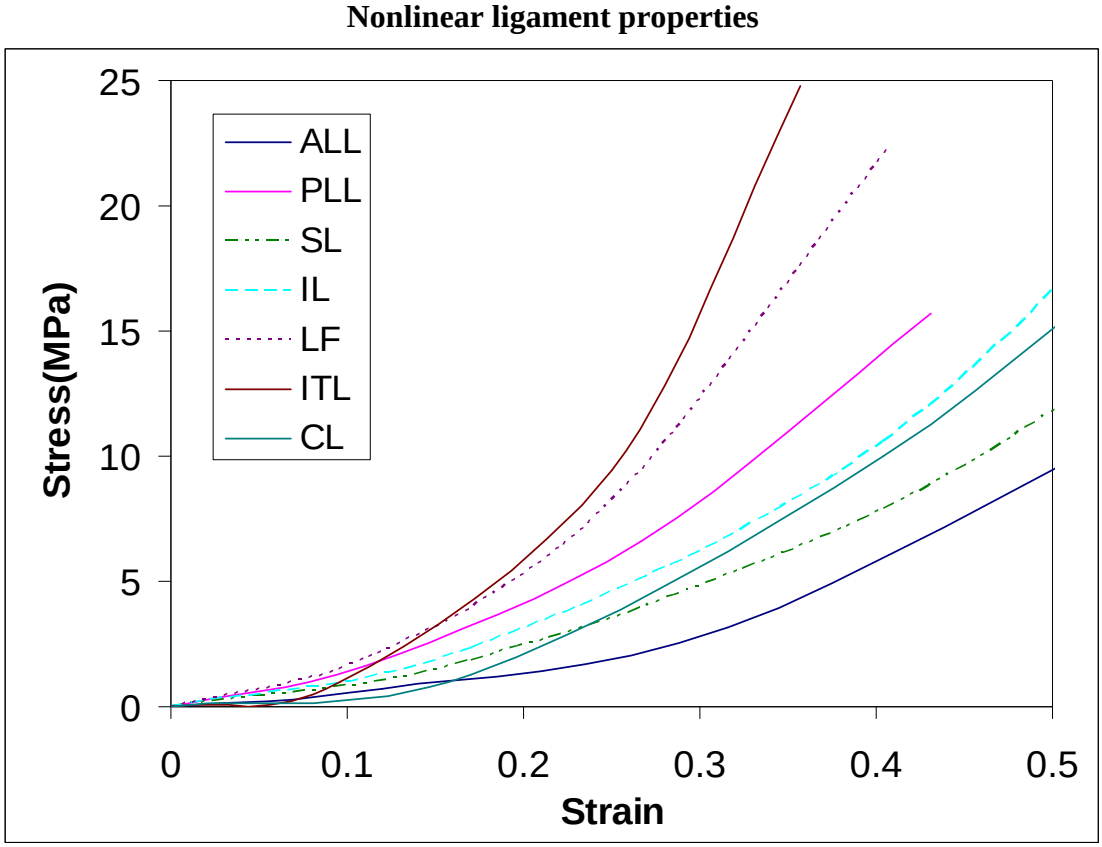

LINEAR **NONLINEAR**

Von Mises Stresses for Compression

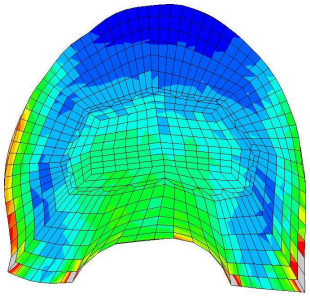

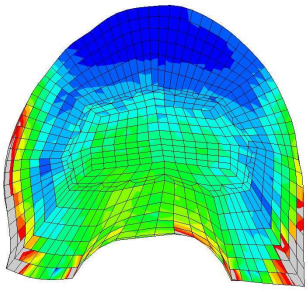

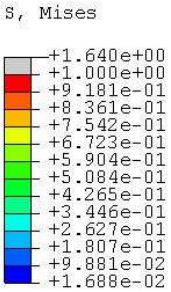

Von Mises Stresses for Flexion

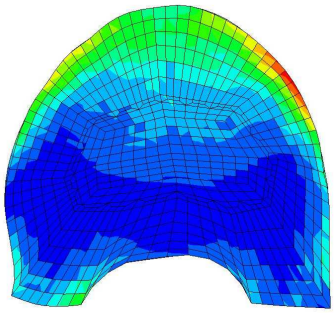

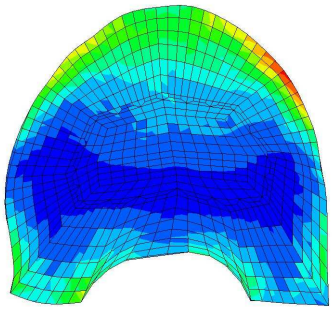

Minimum Principal Strains for Compression

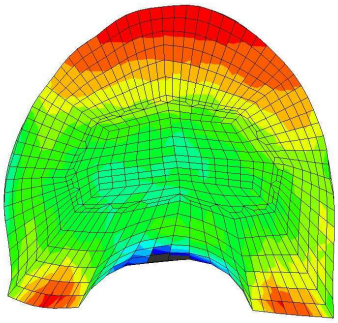

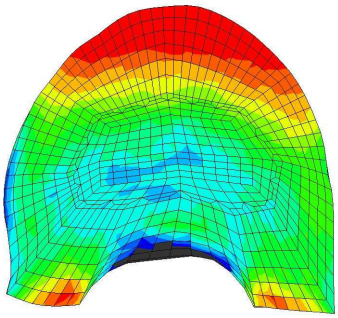

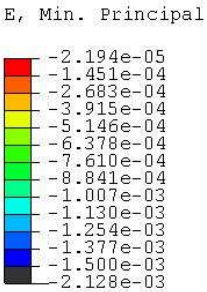

Minimum Principal Strains for Flexion